Appeared without Appendix in
IEEE Transactions on Pattern Analysis and Machine Intelligence
PAMI-15 November 1993

Cahiers de Mathématiques de la Décision, MD
n^o 9124 November 1991
CEREMADE Centre de Recherche de Mathématiques de la Décision.

Finite Element Methods for Active Contour Models and Balloons for 2D and 3D Images [1]

[2]

Laurent D. COHEN and Isaac COHEN

CEREMADE, U.R.A. CNRS 749, Université Paris IX - Dauphine
Place du Marechal de Lattre de Tassigny 75775 Paris CEDEX 16, France.
INRIA, Domaine de Voluceau,
Rocquencourt B.P. 105, 78153 Le Chesnay CEDEX, France.
Email: cohen@bora.inria.fr and isaac@bora.inria.fr

November 5, 1991

Abstract

The use of energy-minimizing curves, known as "snakes" to extract features of interest in images has been introduced by Kass, Witkin and Terzopoulos [23]. A balloon model was introduced in [12] as a way to generalize and solve some of the problems encountered with the original method.

We present a 3D generalization of the balloon model as a 3D deformable surface, which evolves in 3D images. It is deformed under the action of internal and external forces attracting the surface toward detected edgels by means of an attraction potential. We also show properties of energy-minimizing surfaces concerning their relationship with 3D edge points. To solve the minimization problem for a surface, two simplified approaches are shown first, defining a 3D surface as a series of 2D planar curves. Then, after comparing Finite Element Method and Finite Difference Method in the 2D problem, we solve the 3D model using the Finite Element Method yielding greater stability and faster convergence.

We have applied this model for segmenting magnetic resonance images.

[1] This work was partially supported by Digital Equipment Corporation.

[2] We would like to thank **Nicholas AYACHE** and **Robert HUMMEL** for all their help with this paper.

Affiliation of authors:

Laurent D. COHEN is with CEREMADE, U.R.A. CNRS 749,
Université Paris IX - Dauphine,
Place du Marechal de Lattre de Tassigny 75775 Paris CEDEX 16, France.
Email: cohen@bora.inria.fr

Isaac COHEN is with INRIA, Domaine de Voluceau,
Rocquencourt B.P. 105, 78153 Le Chesnay CEDEX, France.
Email: isaac@bora.inria.fr.

Acknowledgments

This work was partially supported by Digital Equipment Corporation. We would like to thank **Nicholas AYACHE** and **Robert HUMMEL** for all their help with this paper.

1 Introduction

We study segmentation of medical 2D and 3D images by making use of "deformable models" [29, 32]. In order to achieve robust segmentation, we introduce a number of enhancements and modifications to the formulation of deformable models. In particular, we define new forces to control the evolution of the deformable model, we formulate the models for true 3D data, and we develop a finite element implementation.

The class of "deformable models" originates with the method of "snakes" introduced by Kass *et al.* [23], which are used to locate smooth curves in 2D imagery. Since then, deformable models have been used for many applications in $2\frac{1}{2}$-D and 3D by Terzopoulos, Witkin and Kass [31, 32] where the deformable surface is constrained to encourage axial symmetry and is evolving under the forces determined from a 2D image or a pair of 2D images. We also make use of deformable surfaces, but the data providing information about the force comes from *true 3D data* sets. We further extend enhancements of the model introduced in [12] for curves to the surface model applications given here.

In [12], we introduced a modification, using "balloons," in order to apply the method of deformable models to stacks of images comprising a 3D data set for an application in segmentation. Our use of deformable models in [12] was limited to the extraction of 2D curves, which were then used to build up a 3D structure. In this paper, we further refine and present the "balloon model," formulating and applying it to true 3D data. For this purpose, we study the use of finite element methods for implementing the solution of the partial differential equations satisfied by the deformable surface. Our application is for the segmentation of 3D magnetic resonance images of crania and heart regions.

We compare different schemes using finite difference and finite element methods to generalize the balloon model introduced in [12] to a 3D cylindrical surface or rectangular patch. In general, these methods are used to reliably extract surfaces in 3D images.

Three dimensional imagery is often represented as a set of intensity voxels (volume elements). A 3D edge detector, after a *local* image analysis [36, 24], provides a set of 3D edgels (edge elements). However, the edgels do not constitute a segmentation. One approach to 3D segmentation involves the integration of 2D segmentation results along slices of the 3D imagery. In this paper, however, we wish to combine information from a 3D edge detector with the method of deformable models applied directly to the solid data.

We are confronted simultaneously with a segmentation problem and a surface reconstruction problem:

(1) We wish to locate edgels belonging to the surface of a single object; this is the

segmentation problem; and

(2) We must represent the surface, together with its differential structure, for subsequent interpretation [1].

Deformable models offer a reasonable approach to solving these problems, due to their stability, controllability, and their property of regularizing data gathered over regions of the image. Regularization techniques, or penalized optimization, are used for many applications in vision (see for example [21, 28, 27, 30] and references there).

In our application, we recover surfaces in 3D medical data, locating surface boundaries of organs and structures, and providing an approximating differentiable description (see Section 6). The differential description may be used for measurements, recognition, visualization, and other purposes [2, 10, 13].

There are two basic approaches to segmentation and image labeling (see Fig. 1). In the classical approach, features are extracted from the image, and a sparse collection of locations and data are obtained; then reconstruction methods are used to interpolate the sparse data to form a representation (and possible segmentation) of the original data. In more recent approaches, such as the method of snakes [23], an initial estimate (such as a curve or surface) is provided, and optimization methods are used to refine the initial estimate based on image data restricted to the region of the evolving estimate. The second approach has the advantage that the feature extraction and representation phases are integrated into a single process, whereas the first approach may make use of prior finely-tuned feature extraction procedures.

In our work, we modify the second approach by incorporating aspects of the first, namely, the evolution of the initial estimate depends not only on local data, but also potentially on the data provided by a distributed sparse collection of feature points such as edgels from a surface edge extractor. Our method, which can make use of a "inflation" or "weight" force, is particularly well suited to noisy data with missing parts such as magnetic resonance images in both two and three dimensions.

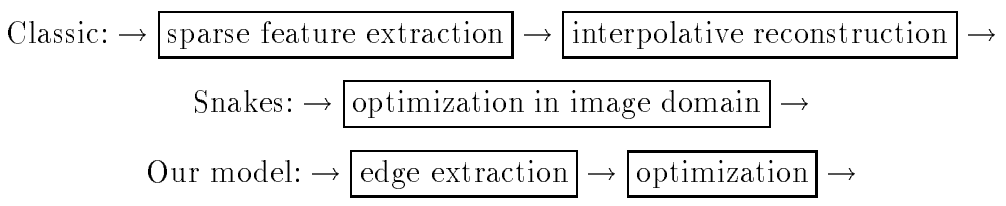

Figure 1: Comparison of reconstruction approaches. Constraints are **explicit** in the first model, **implicit** in the others.

Our method is derived from the original formulation of deformable models [23, 29], but incorporates a number of significant modifications and new features.

In particular, the contributions of our work are the following:

1. We incorporate the use of **edge points** extracted by a local edge detector. This allows us to combine the qualities of a good **local** edge detector, e.g. a Canny-Deriche edge extractor [7, 17, 24], with a **global** active model. This is accomplished by means of an attraction potential generated by convolving a binary edge image with a Gaussian impulse response. The attraction potential can also be defined through the use of a Chamfer distance to edge points.

2. We introduce an internal pressure force by regarding our curve or surface as a **balloon** which is inflated. We add to the previous internal and external forces a **pressure** force pushing out the boundary as if we were introducing air inside. Separately, we make use of a **"weight"** force which simulates gravity. This allows us to be less demanding of the initialization and to give a simpler initial curve or surface.

3. We replace the finite difference method of [12, 23, 30] by a **finite element method** (FEM). With finite differences, we only have knowledge of the functions at discrete points of a subdivision, and have no information between these points. Therefore the distance between successive points must be made very small to achieve sufficient precision so as not to miss too much information, since the external forces are applied at the grid of points. This typically yields large systems of linear equations. Conversely, with the FEM, we work with continuous functions whatever the size of the grid. Therefore, the function under consideration is known everywhere in the image, independently of the chosen discretization. This yields a lower algorithmic complexity and better numerical stability, in our application.

4. We deal with true 3D medical data and use deformable surfaces to extract the surface boundary of organs. We first give a fast approach to solve the 3D problem based on the simultaneous evolution of 2D curves and then give the 3D formulation using the FEM.

We regard the application of deformable-contour models as a method to extract *smooth shapes* in a given region of the image. The philosophy of the approach is to introduce an elastic curve (or surface) in the image, and let it evolve from an initial position under the action of both internal forces (smoothness constraints, and pressure forces) and external forces (attraction towards local edgels and weight forces).

The paper is organized as follows. After recalling the basic principles of "snakes" (Section 2.1) and "balloons," we present enhancements and details about the use of edge data to generate an attraction potential (Section 2.2). We also briefly survey the literature. We then define 3D deformable models (Section 2.3) and give a relationship with 3D edge points (Section 2.4). We show two simplified 3D approaches (Section 3) and then finally solve this minimization problem in both 2D and 3D by a finite element method (Section 4).

We illustrate our technique in the application of the automatic segmentation of medical images. The power of the approach to segment 3D images is demonstrated by a set of experimental results on various complex medical 3D images (Section 5).

2 Energy Minimizing Curves and Surfaces

We first recall some definitions and formulate the mathematical problem. In the following, we will call the active contour model or energy-minimizing curve "the 2D problem" and the active surface model or energy-minimizing surface "the 3D problem."

2.1 2D Active Contour Model

2.1.1 Definition

Snakes are a special case of deformable models as presented in [29]. The deformable contour model is a mapping:

$$\Omega = [0,1] \rightarrow I\!R^2$$

$$s \mapsto v(s) = (x(s), y(s))$$

We define a deformable model as a space of admissible deformations $\mathcal{A}$ and a functional E. This functional represents the energy of the model which will be minimized and has the following form:

$$E : \mathcal{A} \rightarrow I\!R$$

$$v \mapsto E(v) = \int_\Omega w_1 \|v'(s)\|^2 + w_2 \|v''(s)\|^2 + P(v(s))ds$$

where v' and v'' denote derivatives of v and where P is the potential associated to the external forces. The potential is computed as a function of the image data according to the desired goal. If we want the snake to be attracted to edge points, the potential should depend on the gradient of the image. In the following, the space of admissible

deformations $\mathcal{A}$ is restricted by the boundary conditions $v(0)$,$v'(0)$,$v(1)$ and $v'(1)$ being given. We can also use periodic curves or other types of boundary conditions.

The mechanical properties of the model are controlled by the functions w_j. Their choice determines the elasticity and rigidity of the model.

If v is a local minimum for E, it satisfies the associated Euler-Lagrange equation:

$$\begin{cases} -(w_1 v')' + (w_2 v'')'' + \nabla P(v) = 0 \\ v(0), v'(0), v(1) \text{ and } v'(1) \text{ given.} \end{cases} \tag{1}$$

In this formulation each term appears as a force applied to the curve. A solution can be viewed either as realizing the equilibrium of the forces in the equation or reaching the minimum of the energy.

Thus the curve is under control of two types of forces:

- The internal forces (the first two terms) which impose the regularity of the curve. The constants w_1 and w_2 impose the elasticity and rigidity of the curve.

- The image force (the potential term) pushes the curve to the significant lines which correspond to the desired attributes. It is defined by a potential of the form $\int_0^1 P(v(s))ds$ where
$$P(v) = -\|\nabla I(v)\|^2.$$
Here, I denotes the image. The curve is then attracted by the local minima of the potential, which means the local maxima of the gradient, i.e. edges (see [19] for a more complete discussion of the relationship between minimizing the energy and locating contours).

Other forces can be added to impose constraints defined by the user. We will make use of additional forces.

2.1.2 Finite Difference Solution

We first formulate the discretization of the equation by finite differences following [23] in a more succinct fashion. Setting $F(v) = (F_1(v), F_2(v)) = -\nabla P(v) + F_{other}$, the sum of image and other external forces, the equation

$$-(w_1 v')' + (w_2 v'')'' = F(v), \tag{2}$$

becomes a linear system after applying finite differences in space:

$$AV = F.$$

Here A is pentadiagonal and V and F denote the vectors of positions $v_i = v(ih)$ and forces at these points $F(v_i)$ respectively.

Since the energy is not convex, there may be many local minima of E.

Finding the global minimum of the energy does not necessarily have a meaning. Indeed, if v_m is a point of the plane where P has a global minimum, then the constant curve $v(s) = v_m$ is a global minimum for the energy with periodic boundary conditions.

But we are interested in finding a good contour in a given area. We suppose in fact that we have a rough estimate of the curve. We impose the condition to be "close" to this initial data by solving the associated evolution equation

$$\begin{cases} \dfrac{\partial v}{\partial t} - (w_1 v')' + (w_2 v'')'' = F(v), \\ v(0,s) = v_0(s), \\ v(t,0) = v_0(0), \quad v(t,1) = v_0(1), \\ v'(t,0) = v_0'(0), \quad v'(t,1) = v_0'(1). \end{cases} \tag{3}$$

where v' denotes differentiation with respect to s. A solution to the static problem (2) is achieved when the solution $v(t)$ stabilizes. This is because the term $\dfrac{\partial v}{\partial t}$ tends to 0 (generally) and the dynamic system (3) reduces to (2) at infinity.

After formulating the evolution problem using finite differences with time step τ and space step h we obtain a system of the form

$$(\mathcal{I} + \tau A)v^t = (v^{t-1} + \tau F(v^{t-1})), \tag{4}$$

where $\mathcal{I}$ denotes the identity matrix. Thus, we obtain a linear system and we have to solve a pentadiagonal banded symmetric positive system. We compute the solution using a LU decomposition of $(\mathcal{I} + \tau A)$. The decomposition needs be computed only once if the w_i remain constant through time. We stop iterating when the difference between two successive iterations is sufficiently small. After each iteration we test $\|v_t - v_{t-1}\|$ and stop if it is lower than a given threshold. Of course, the lower the threshold, the better we can be sure it is a real equilibrium.

Moreover, the linear system above is such that each row of the matrix $(\mathcal{I} + \tau A)$ is obtained by circularly shifting the previous one. The product of a matrix of this form and a vector can be viewed as the convolution of a row of the matrix with the vector. Since derivatives are at most of the fourth order, this corresponds to a convolution of the discretized curve v_i by a kernel of length five. This smoothing can in fact be viewed as a 1D low-pass filter on the curve.

Note that in Eqn. (4), v^t has two components x^t and y^t, and we can write separately the two equations satisfied by the vectors x^t and y^t. These equations are independent

except for the term $(F_1(v), F_2(v))$ where x and y cannot be separated. However, as we will see later, in all the iterative schemes we use in this paper, the term $F(v)$ is explicit. This means that at each iteration it may be considered as a constant vector and the two equations satisfied by x and y can be computed separately. Accordingly, we sometimes consider the equation for the unknown v as a scalar function, instead of a two- or three-component vector equation.

The finite difference formulation of the problem makes the curve behave like a set of masses linked by springs of zero length (when fully contracted). Consequently, if there is no image force ($F = 0$), then either the curve shrinks and vanishes to a point, or it straightens out to become a line depending on the boundary conditions.

If the spatial discretization step h along the curve is more than 2 pixels, the curve can either jump across edges or fail to be attracted to edges. This means that the number of nodes must be of the order of the length of the curve.

The coefficients of elasticity and rigidity have a great effect on the behavior of the evolution of the curve along time iterations. If w_1 and w_2 are close to unity, the internal energy E_{int} has a major influence and the image forces have small effect. In this case the initial curve is merely smoothed due to the regularization action. We are currently studying the effect of these coefficients in simple cases to evaluate the ability of the model to detect corners.

A correct choice for parameters is guided by numerical analysis considerations. We want the coefficients within the rigidity matrix A to have similar orders of magnitude. We obtain good results when the parameters are of the order of h^2 for w_1 and h^4 for w_2, where h is the space discretization step.

2.2 Improving the Model. The Balloon Model

The potential P is such that the force $F(v) = -\nabla P(v)$ generates the attraction of the curve or surface to the image regions that we seek to extract. Our main goal is the extraction of "good" edge points (i.e., to be able to remove spurious edge points, while insuring connected contours).

The formulation described in the previous section leads to certain difficulties, for which one of us proposed a variation (in [12]) by defining new forces and a potential function. In the following sections, we will extend in a natural way these revised forces for use with the Finite Element Method for both 2D curves and 3D surfaces. In the subsection immediately following, we summarize the main points developed in 2D in [12], elaborating on certain important details. All these points are identical for a surface evolving in a 3D

image.

2.2.1 Normalization of the Force

The external forces based on image data applied to the curve to push it to the high gradient regions are modified to give more stable results. Indeed, it is not possible to choose a uniform time step τ suitable for all points of the contour. If τ is too large, some points on the curve may move too quickly, and jump across the desired minimum and never come back. If τ is too small, very few high gradient points will attract the curve.

So instead of modifying the time step, we modify the force by normalizing it, taking $F = -k\frac{\nabla P}{\|\nabla P\|}$. This simulates a local time step which makes the curve evolve at the same speed everywhere.

2.2.2 The Balloon Model. The Weight Force

To make the snake find its way, an initial guess of the contour has to be provided manually. This has many consequences on the evolution of the curve (or surface).

- If the curve is not close enough to an edge, it is not attracted to it.
- If the curve is not subjected to any counterbalancing forces, it tends to shrink on itself.

Accordingly, we introduce an internal pressure by considering our curve as a **balloon** which is inflated. The **pressure** force is added to the internal and external forces to push the curve outward, as if we were introducing air inside. The curve both expands and is attracted to edges as before. But if the edge is too small or too weak with respect to the pressure force, the curve passes over the edge, growing outward.

The internal pressure force prevents the curve from being "trapped" by spurious isolated edge points, and makes the final result much less sensitive to the initial conditions.

The force F now becomes

$$F = k_1\vec{n}(s) - k\frac{\nabla P}{\|\nabla P\|}(v(s)) \tag{5}$$

where $\vec{n}(s)$ is the unit vector normal to the curve at point $v(s)$ and k_1 is the amplitude of this force. The coefficients k_1 and k are chosen such that they are of the same order, which is smaller than a pixel size (the length unit), with k slightly larger than k_1, so an edge point can stop the inflation force.

Remark that this force can also be interpreted as the gradient of an extra energy term. This would be a surface term $E_{area} = -k_1 \int dA$, measuring the area inside the region

delimited by the curve. Minimizing this energy corresponds to have the inside region as large as possible, which is obtained by a force pushing in the direction of the external normal.

Note that F depends on not only the position $v(s)$, but also of the normal at this position. In the iterative methods presented in this paper, we solve problems formulated under the assumption that F depends on the position v, but not on derivatives. This assumption is made possible by using as an approximation to v^t at step t the previously computed value v^{t-1}.

Suppose we have an image of a black rectangle on a white background, and a curve is placed inside the rectangle. Without the inflation force, even if we have perfect edge detection, the curve will shrink and vanish. Starting from the same small curve, but using the inflation force, we obtain the entire rectangle (see Fig. 4). When the balloon reaches equilibrium, the points that are attracted to image edges are slightly outside of the real contour. We thus reduce the inflation force to localize the final position of the curve.

As another example, we apply the technique to a slice from a 3D image of the region of the heart obtained with Magnetic Resonance Imaging (MRI). We wish to extract the left ventricle. We use here the 3D edge detector [24] obtained by generalization of the 2D Canny-Deriche filter. In Fig. 7 we show the result of the application of balloons to detect the ventricle. The initial curve was neither close in shape nor in position to the actual ventricle.

One aspect of the increased complexity of the method is a large variation of the length of the curve between the initial data and the final limit curve. As we remarked above, the number of nodes along the curve should be approximately equal to the length of the curve. Thus we must change the discretization during the iteration process. To do this, we periodically reparametrize the curve, and resample node points. This means that we construct a new parametrization using the existing curve by sampling at a one pixel distance between nodes. This also prevents nodes from clustering at high gradient points and from separating, creating a large space between some nodes.

Since the length changes, we must change the matrix A during the iteration process. Accordingly, our algorithm incorporating internal pressure takes more time to converge, since we must compute matrix inverses at each reparametrization and also since we begin with a curve very far from the solution. The added computation time is a price we must pay for the simplicity of specifying a coarse initial curve.

In the same spirit as the balloon model, we will also incorporate a "**weight force**" into the 3D reconstruction models. The weight force allows us to take a very simple initial surface placed on the border of the image. The surface then "falls" under the influence

of the "gravity," to catch an object which might be far from the border. If we instead attempt to locate a surface by surrounding the outside of the object by the deformable model and then use a "deflation" force (identical to the inflation force, but with a negative k_1), instability can result since the surface may then self-intersect after a few iterations.

The "weight force" is uniform on the surface in direction and intensity: $F = k_1\vec{Z}$. The initial surface is typically a plane on one side of the 3D image, and $\vec{Z}$ is defined to be normal to this plane. As with the inflation force, if the weight force is not turned off at the end of the process, equilibrium is reached with the surface slightly shifted from the desired solution. In the weight force case, however, we eliminate the force locally at a point when an area of large variation of the gradient is reached instead of once global convergence is obtained for the pressure force. This modification improves the progression to the solution. As a result, we may use larger values of k_1 and thus move faster without missing the solution. As with the balloon model (see [12]), the surface is not stopped by isolated spurious points. The effect of the weight force will be demonstrated in Figs. 19, 20 and 21.

2.2.3 Accounting for Prior Local Edge Detection: Attraction Potential

We make use of **edge points** extracted prior to the use of the deformable model by a local edge detector. In 2D, edge points tend to lie along curves, and in 3D they are located on surfaces. Accordingly, we are able to combine the qualities of a good **local** edge detector, such as the Canny-Deriche edge extractor [7, 17, 24], with a **global** active model. We must define the attraction forces through the use of a potential function. The potential may be defined by convolving the binary edge image with a Gaussian impulse response. An example is shown in Fig. 5, plotting the potential surface generated by the rectangle image of the previous section (Fig. 4).

We also used in [13] a Chamfer distance that approximates the Euclidian distance to the nearest edgels [5], or a Euclidean distance image (as defined in [15]). Fig. 6 shows a potential based on the latter distance map for the same rectangle image as before. These approximate distance metrics are of interest because they can be obtained by a fast algorithm, requiring only two-passes through the binary image.

We denote by $d(v)$ the distance between a point v and the nearest edge. In general, a large class of potentials may be formulated as $P(v) = g(d(v))$, i.e., as a function of the distance to the closest contour. For instance,

$$P(v) = -e^{-d(v)^2}$$

produces a potential that is similar to the Gaussian convolution method discussed above,

except that only the closest edge point has an effect at a position v. The potential

$$P(v) = \frac{-1}{d(v)} \quad , \quad (P \equiv -1 \text{ if } \ d(v(s,r)) < 1),$$

where the unit distance is the pixel size, produces a faster convergence since this potential decays more slowly, producing larger forces at points distant from the edges.

Remark that if the potential is defined by $P(v) = g(d(v))$, the force becomes $F(v) = -\nabla P(v) = -g'(d(v))\nabla d(v)$. When this force is normalized as suggested in subsection 2.2.1 above, we have $F = -k\frac{\nabla d}{\|\nabla d\|}$. The formula does not depend on function g but the numerical result may be different because of machine accuracy. So, when we normalize the force, we could take any function g easy to compute, for example $g(d) = d$, but the distance function is not differentiable everywhere. This is why g usually behaves like d^2 for small d to avoid problems at points where $d = 0$. In general, g is also used to regularize the distance function d.

However, in the case of a potential defined from a distance function, it may be better when the force is not normalized and the norm of F depends on $g'(d)$ and $\|\nabla d(v)\|$. Using the triangular inequality, we can see that $\|\nabla d(v)\| \leq 1$. So, a good choice of g permits to control the norm of the attraction force when d is small or large. This will be discussed in the following.

The attraction forces derived from the potential may be used either as the only image forces, or may be combined with an intensity-gradient image to enhance the detected edges. The latter approach is useful when the detected edges are broken into small disconnected segments.

The methods of convolving edges with a Gaussian and defining a function of $d(v)$ were used by us in [11, 12] and [13]. However, the attraction potential defined by Weiss [34], and the weak-continuity method of Blake and Zisserman [4], are closely related. The attraction potential and weak-continuity methods are applied to sparse isolated points, our set of edge points are extracted by a local edge detector, and thus may contain full curves (or surfaces in 3D). Moreover, in these methods, the model tries to match the whole data, while we are doing segmentation at the same time. Our deformable model has to find out which parts of the data to stick to. Also, the goals are different. The property of the varying mesh model is to define automatically an optimal mesh to deal better with corner reconstruction, using an extra potential term. In our model, the inflation force is a powerful tool to make the model converge to the solution being less demanding of the initialization. These two tools could be associated together to obtain both properties.

In the next section we survey more closely the definition of attraction potential in the reconstruction literature.

2.2.4 A Survey of Attraction Potential used in Reconstruction Methods

The general formulation of the problem as presented in [34] uses Tikhonov regularization [33] to approximate data g by a smooth function f, in order to reconstruct a curve or a surface. We use a second order regularization scheme to insure a $\mathcal{C}^1$ continuity of the solution. Two terms are minimized:

- A criteria of the faithfulness to the data; and
- A regularizing term containing derivatives of the function.

The energy functional can be written in the form:

$$E(f,g) = \int V(f(s),g(s))ds + \int S(f(s))ds \tag{6}$$

where V is a measure of the distance between the function f and the data g, and $S(f)$ measures the smoothness of the reconstruction f. Similar to our potential P, the attraction force is obtained from the gradient of V, $F_V = -\nabla V$.

Let us consider the case of a curve $f(s) = (x(s), y(s))$ and discuss the different approaches to reconstruction. We also give an interpretation of the forces by means of zero-length spring attraction forces. All of our discussion generalizes naturally to surfaces in 3D data.

Least-squares. Explicit constraints. The most classic problem is least-square fitting given the position of the curve at a collection of points $f_i = f(s_i) = (x_i, y_i)$ at known values of the parameter s_i. We use as an attraction potential

$$V(f) = \sum_i \|f(s_i) - f_i\|^2,$$

(see, for example, [28, 25] and their references). The case of a *cartesian curve* is especially simple since $x_i = s_i = x(s_i), x(s) = s$ and $V(f) = \sum_i (y(s_i) - y_i)^2$; this is the case treated in [25].

The attraction force obtained by differentiation of the potential is proportional to the distance between a data point f_i and the value of f at s_i. We can interpret this force physically as a spring (which contracts to zero length) connecting a point of the curve (or surface) $f(s_i)$ and the given point $f_i = (x_i, y_i)$. Each node of the curve is connected by a spring to one **explicit** data point. Thus each data point (x_i, y_i) influences the force at only one point of the curve. The curve is constrained to best fit to **all** the data. Moreover, the data points must be sorted in a natural order. This is the case for a cartesian curve (or surface), where values s_i correspond to positions

along an axis (two axes for a surface). For a general curve, given a collection of (x_i, y_i) data, the natural order of the points may not be so apparent.

Position-independent. Implicit constraints. When the s_i are not given and the curve has to best fit the set of points f_i, a simple extension of the previous idea would define an attraction potential simulating a zero-length spring for each data point of the plane which has effect for any point of the curve. At a point h of the plane, the potential is the sum of the contributions of all the f_i: $V(h) = \sum_i \|h - f_i\|^2$. The potential V thus may be viewed as a convolution of the sum of Dirac masses δ_{f_i} at the data points f_i with the function $\|h\|^2$:

$$V(h) = \int \sum_i \delta_{f_i}(u)\|h - u\|^2 du = \sum_i \|h - f_i\|^2.$$

This potential has the advantage of being convex, but does not work out well since a point of the curve will be attracted with the strongest force by the most remote data point. Indeed the only minimum is a curve reduced to a point located at the mean value of the f_i's.

Our approach convolves a binary image of edge points with a function of the form $-e^{-\|h\|^2}$, while Weiss in [34] convolves a set of sparse data points with a similar function of the form $\frac{-ae^{-\|h\|^2/b^2}}{1+c\|h\|}$. We chose a negative Gaussian function since it behaves like $C + \|h\|^2$ for small h (where C is a constant) and has a zero limit at infinity. Thus, the attraction force behaves like a zero-length spring when h is small, and when h becomes large the force decreases to zero. So the curve is most attracted by the points close to it, and distant points have no attraction force.

Blake and Zisserman's functions $g_{\alpha,\lambda}$ and $g^*_{\alpha,\lambda}$ of [4] (Fig. 7.1) are likewise similar in structure. However, their forces are used to define the internal attraction between two successive points in a discretized curve. The idea of the weak continuity is that if the variation is too large at some point of the curve, then it is better to break the reconstruction curve there and introduce a discontinuity. The weak continuity makes springs defining the internal attraction force (see subsection 2.1.2) break if they get too long. The attraction force based on the image data that we use here is thus similar to the internal attraction force in the weak continuity model of [4].

Note that the attraction force for the convolution-based potential allows the curve (or surface) to choose among the data points the ones to fit. Each point of the curve is attracted by all the data **points close enough** to it.

When we define the potential by $P(v) = -e^{-d(v)^2}$ using the Chamfer distance [13], each point is attracted only by the closest edge point. The curve behaves as though

each point is linked by a weak spring (which breaks if too long) to the **closest data point**. The constraints in this part are not known explicitly like in the "classic" reconstruction but defined **implicitly** by the relative position of a node to the data.

"Snakes." In some cases, the data is not known explicitly. For example, the potential introduced with the snakes in [23] is based on the property of edge points to have a large image-gradient value. The potential defined as a function of the image-gradient results in the curve being attracted to the high gradient points without explicit knowledge of these points. The constraints are also **implicit** in this case. In the snake approach, the data points are located directly by the curve through the minimization of the potential (see Section 2.1). Moreover, all the points of the curve are influenced by the attraction forces from the image.

Mixed version. Recently a combination of the previous approaches was proposed in [16]. Two potentials are defined. A "data energy" term is used to represent an attraction of the surface to the closest data point, which yields a force that is linear when close to the data and decreases to zero when far from the point. The data energy is the same as our potential using the Chamfer distance. A "feature energy" term represents an attraction to feature points. Though the function of convolution is slightly different in form, it has similar properties to the "weak spring" model discussed above. The main difference is that this "feature potential" is modified with iterations. The threshold at which the spring breaks decreases from a reference distance when $t = 0$ to zero when $t = T_0$. Therefore, the influence of features decreases during the evolution.

In this section, we presented the enhancements of our model, normalizing the force to get more stability, adding an inflation or weight force to push the model more quickly to the solution, and defining an attraction potential making use of edge points extracted prior to the application of the model. For this last point, we gave a survey of the related attraction potential found in the literature.

We will make use, in this paper, of all the features presented so far for 2D curves as well as 3D surfaces.

2.3 3D Active Surface Model

The 3D model is obtained by generalizing the formulations given in the previous sections. A surface $\mathcal{S}$ is defined by a mapping v:

$$v : \Omega = [0,1] \times [0,1] \rightarrow I\!R^3$$

$$(s,r) \mapsto v(s,r) = (v_1(s,r), v_2(s,r), v_3(s,r))$$

and the associated energy E is defined on an admissible class $\mathcal{A}$ of mappings v, and has form:

$$E : \mathcal{A} \to I\!R$$

$$v \mapsto E(v) = \int_\Omega w_{10} \left\| \frac{\partial v}{\partial s} \right\|^2 + w_{01} \left\| \frac{\partial v}{\partial r} \right\|^2$$

$$+ 2w_{11} \left\| \frac{\partial^2 v}{\partial s \partial r} \right\|^2 + w_{20} \left\| \frac{\partial^2 v}{\partial s^2} \right\|^2 + w_{02} \left\| \frac{\partial^2 v}{\partial r^2} \right\|^2 + P(v(s,r)) ds\, dr \tag{7}$$

where $P(v(s,r)) = -\|\nabla I(v(s,r))\|^2$ is the potential associated with the external forces. The internal forces acting on the shape of the surface depend on the coefficients w_{ij} such that the elasticity is determined by (w_{10},w_{01}), the rigidity by (w_{20},w_{02}), and the resistance to twist by (w_{11}). That is, the coefficients determine the mechanical properties of the surface. We can also constrain the surface structure by adjusting boundary conditions (for instance, to create a cylinder or a torus). This model, restricted to its first-order derivative terms, may be interpreted physically as a membrane, and with inclusion of second-order derivative terms may be interpreted as a thin plate.

A local minimum v of E satisfies the associated Euler-Lagrange equation:

$$\begin{cases} -\frac{\partial}{\partial s}\left(w_{10}\frac{\partial v}{\partial s}\right) - \frac{\partial}{\partial r}\left(w_{01}\frac{\partial v}{\partial r}\right) + 2\frac{\partial^2}{\partial s \partial r}\left(w_{11}\frac{\partial^2 v}{\partial s \partial r}\right) \\ +\frac{\partial^2}{\partial s^2}\left(w_{20}\frac{\partial^2 v}{\partial s^2}\right) + \frac{\partial^2}{\partial r^2}\left(w_{02}\frac{\partial^2 v}{\partial r^2}\right) = F(v) \end{cases} \tag{8}$$

subject to boundary conditions. The Euler-Lagrange equation is a necessary condition for a minimum. As with Eqn. 5, F denotes the sum of forces: $F = F_{image} + F_{balloon}$, F_{image} is the force obtained after normalization from the gradient of the attraction potential, and $F_{balloon}$ is either the inflation or weight force. Since the energy function is not convex, there may be many local minima of E. The Euler-Lagrange equation (Eqn. 8) is satisfied at any such local minimum. But as we are interested in finding a 3D contour in a given area, we assume in fact that we have a rough *prior* estimation of the surface. This estimate is used as initial data for the associated evolution equation, in which we add a temporal parameter t:

$$\begin{cases} \frac{\partial v}{\partial t} - \frac{\partial}{\partial s}\left(w_{10}\frac{\partial v}{\partial s}\right) - \frac{\partial}{\partial r}\left(w_{01}\frac{\partial v}{\partial r}\right) + 2\frac{\partial^2}{\partial s \partial r}\left(w_{11}\frac{\partial^2 v}{\partial s \partial r}\right) \\ +\frac{\partial^2}{\partial s^2}\left(w_{20}\frac{\partial^2 v}{\partial s^2}\right) + \frac{\partial^2}{\partial r^2}\left(w_{02}\frac{\partial^2 v}{\partial r^2}\right) = F(v), \\ v(0,s,r) = v_0(s,r) \ \text{ (initial estimate)}, \end{cases} \tag{9}$$

and where boundary conditions may have to be imposed (additionally). A solution to the static problem is found when the solution $v(t,s,r)$ converges as t tends to infinity.

Assuming sufficient uniform convergence is achieved, the term $\frac{\partial v}{\partial t}$ vanishes, thus providing a solution of the static problem.

With this formulation, and with the potential as given above, the resulting surface will accurately locate the 3D edge points.

Before describing the numerical solutions of the 3D reconstruction we give in the next section a mathematical result showing how the surface locates on the Canny's 3D edge surfaces.

2.4 Minimizing Surfaces and 3D Image Edge Points

We comment on the relationship between the surface minimizing the energy of external forces E_{image} and 3D edge points. A similar formulation for planar curves is given by Fua and Leclerc [19]. Recall that the external energy is given by

$$E_{image} = \int\int P(v(s,r))dsdr.$$

We use the following definition of the 3D edges, as proposed by Canny [7]:

Definition 1 *A 3D edge is a surface $\mathcal{S}$ whose points have a minimal potential in the direction normal to the surface. All points along the surface $\mathcal{S}$ satisfy:*

$$D_{N(v(s,r))}P(v(s,r)) = 0 \tag{10}$$

where $N(v(s,r))$ is the normal to the surface $\mathcal{S}$ parametrized by $v(s,r)$, D_N is the directional derivative in the direction N, and P is the potential to be minimized.

When the potential is defined in terms of the image gradient ∇I (where typically, I is replaced with a Gaussian-convolved version of the image), the former definition is the same as Canny's edge points:

Definition 2 *A 3D Canny edge is a surface $\mathcal{S}$ whose points have a maximal gradient magnitude in the direction normal to the surface. All points along the surface $\mathcal{S}$ (called Canny's edge points) satisfy:*

$$D_{N(v(s,r))} \|\nabla I(v(s,r))\| = 0 \tag{11}$$

where ∇I is the gradient magnitude.

To explore the relation between the energy minimizing surfaces and this definition, let us define the energy associated to the external forces as

$$E_P(\mathcal{S}) = \frac{1}{|\mathcal{S}|}\int\int P(v(s,r))dA, \tag{12}$$

where $|\mathcal{S}| = \int\int \|v_s \wedge v_r\| \, dsdr$ is the surface area and $dA = \sqrt{EG - F^2} dsdr$ is the standard surface area measure.

In [14] we show that a surface $\mathcal{S}$ is a local minimum of E_P, with respect to infinitesimal deformation, if:

$$D_{N(v(s,r))} P(v(s,r)) = \frac{eG - 2fF + gE}{EG - F^2} \left(P(v(s,r)) - \frac{1}{|\mathcal{S}|} \int \; P(v(s,r)) dA \right), \qquad (13)$$

where $E(s,r)$, $G(s,r)$, $F(s,r)$, $e(s,r)$, $f(s,r)$ and $g(s,r)$ are the coefficients of the first and second fundamental forms in the basis $\{x_s, x_r, N\}$ (using the same notation as in [18]). A remarkable result is that the quotient $\frac{1}{2}\frac{eG - 2fF + gE}{EG - F^2}$ is simply the mean curvature of the surface $\mathcal{S}$.

Eqn. 13 shows that there exists two interesting special cases:

(1) If a minimizer of E_P is a minimal surface (i.e., a surface with a mean-curvature which is everywhere zero), then it is automatically a 3D edge;

(2) If the minimizing surface is composed of edgels with constant Potential, then the term within parentheses in Eqn. 13 vanishes, and the surface is again a 3D edge.

In general, these are interesting but exceptional academic situations, and the deformable model simply converges to a solution which is a balance between the applied external forces (corresponding to the energy E_P) and the internal forces, parametrized by the elasticity coefficients w_{ij}. The directional derivative will satisfy Eqn. 13, but not in general be zero. But in practical implementation, this is approximately the case when the surface is smooth or when the potential has small variation along the surface.

3 Simplified 3D Model

The main difficulty in passing from modeling curves in 2D to modeling surfaces in 3D is the very significant growth of the computation time due to the size of the system to solve. In this section, we describe a much-simplified 3D surface model, with the aim of minimizing the computational requirements.

A 3D image is viewed as a sequence of 2D images which we call slices or cross sections. In this section, we first present a 3D reconstruction method based on successive solutions of 2D problems, then show how the 3D deformable model may be simplified to a simultaneous solution of 2D problems interacting to yield a fast algorithm.

3.1 3D Reconstruction from a Sequence of 2D Contour Models

In [12], we reported initial experiments with 3D reconstruction using a method that directly extends the 2D method. In this work, we extracted the contour slice by slice. For each slice, a 2D model is applied. In order to improve the speed of the algorithm, the result of the previous slice is used for solving the successive slices. Assuming that the variations are small from one slice to the next, this works well, in the same way that snakes are used for temporal tracking in [22, 23].

In order to reconstruct the entire 3D surface, we initialize the process using a curve obtained from the balloon model in an intermediate cross section, and then propagate the result to neighboring cross-sections. In [1] a related approach was taken, but successive curves were extracted by hand from each slice, using an edge image from each slice. Note that the inflation force is necessary only for the first slice, to have a good solution on that slice, beginning with a bad initial data. But in the following slices, the inflation force is not used since the solution of the previous slice is already close to the solution of the current slice.

Fig. 8 and 9 shows a reconstruction of the left and right ventricles using data from a 3D magnetic resonance image of the heart region. This reconstruction is nearly automatic, although when the contour undergoes a large change from one slice to the next, the initial curve in that slice may have to be redefined in order to obtain a good contour. This problem can be ameliorated by adding interpolation slices when necessary. We note that the problem never occurs in practice when the image resolution is the same in the three axes.

The entire 3D surface represented as a sequence of contours of the slices. We use the NUAGES software package (see [1]) to display the results, which also has the capability to define a 3D surface from planar curves.

The main issues of that approach are that first, there is no interaction between slices and second, the surface has to be cylindrical. The first point is solved in next section while the second will need the general model of Section 4

3.2 Fast Solution of the 3D Constrained Problem

We next describe a fast approach to solve the 3D problem based on the simultaneous evolution of 2D curves.

The 3D deformable model is obtained by minimizing the energy term Eqn. 7 defined in Section 2.3 which uses parametrized surfaces $v(x) = v(s,r) = (v_1(s,r), v_2(s,r), v_3(s,r))$.

In order to keep the model simple, we limit degrees of freedom of the deformation to two

components instead of three by constraining the third component v_3, which corresponds to the slice level, to depend only on r. In this case, the third component of the external force is zero.

Thus the surface that we seek is represented as a sequence of planar curves, with the second parameter r being the index of the slice. We have $v(s,r) = (v_1(s,r), v_2(s,r), r)$ so that for each fixed value of the parameter r, there corresponds a closed curve parametrized by s lying in a slice of the 3D image.

The consequences of constraining the surface as a sequence of plane curves entails two advantageous simplifications:

- First, the curves of the representation are necessarily separated, and undesirable deformations which would require a new parametrization of the surface are avoided. Although this imposes a restriction on the surfaces that we can reconstruct, the representation involves distinct curves, one per slice. As a result, if a contour is missing in a slice, the surface nonetheless bridges the neighboring contours, creating a smooth surface.

- Second, the extraction of information within a slice is simplified, both during the iterative construction as well as for the final result, since the surface is represented by slices. In the more general case, where nodes can move between slices, it is nontrivial to compute the contours resulting from the intersection of the surface and a slice. In the approach we present at the end of the paper for the general 3D model, we in fact make use of such a computation for visualization of information on slices.

The main difference between the slice-by-slice approach of the previous section and the constrained 3D approach of this section is first, that an interaction is permitted between neighboring slices and also their simultaneous evolution. If edges are missing in a particular slice, then the previous method will fail, whereas using $v(s,r)$ opens the possibility that edges missing from a sequence of slices will be filled in. We can see in Figs. 10 and 11 how such missing edges are retrieved. This is illustrated by the bottom middle slice in Fig. 11 where a 2D deformable model would not reconstruct the missing edges. It would only smooth the data and give a small rectangle corresponding to the available edges. With the simplified 3D model, the curve on one slice is also attracted by the edge data of the neighboring slices, and this helps to reconstruct the whole curve (a square in the example).

We recall that the solution is obtained by minimizing the energy of (7). A minimum v of the energy satisfies the Euler equation 8, and a solution to the static problem is found when the solution $v(t)$ of 9 stabilizes. In fact, since $v_3(s,r) = r$, only the first two

components of Eqns. 8 and 9 are nonzero. Solving this equation with finite differences, we obtain a 2D linear system of the form:

$$\frac{V^t - V^{t-1}}{\tau} + AV^t = F(V^t), \tag{14}$$

where V^t is the vector whose components are the values of $(v_1(s,r), v_2(s,r))$ at the nodes of the discretization at iteration t. The first unknown vector V^0 is given by the initial data. Assuming V^{t-1} calculated, we solve Eqn. 14 with respect to V^t.

The unknown V^t appears in the three terms of Eqn. 14. We say that the scheme is *totally implicit*. It is difficult to solve since the force F has a complicated form. We can approximate V^t by V^{t-1} in the term $F(V^t)$, like in the 2D case (Eqn. 4). We then say that we solve a *semi-implicit* scheme, i.e., one that is explicit in the force term (F) and implicit for the matrix term A. This will also be the case for the finite element method, discussed in the following sections. Inversion of the 3D scheme of this section is obtained by solving the system

$$V^t = (\mathcal{I} + \tau A)^{-1}(V^{t-1} + \tau F(V^{t-1})).$$

It is easier, and thus faster, to solve the *totally explicit* scheme where the term AV^t is also approached by the known value AV^{t-1}. The unknown V^t is then directly calculated without matrix inversion by the formula:

$$V^t = (\mathcal{I} - \tau A)V^{t-1} + \tau F(V^{t-1}).$$

Note that this explicit scheme is a first order development of $(\mathcal{I} + \tau A)^{-1}$ as $(\mathcal{I} - \tau A)$. In practice, both $(\mathcal{I} + \tau A)^{-1}$ and $(\mathcal{I} - \tau A)$ perform a smoothing operation on the data V^{t-1}. So, in our implementation, we first add the forces at each iteration, and then smooth v to remove singularities. This does not change the global behavior and gives, at each iteration, a better estimation for visualization of the intermediate results.

There is a certain anisotropy introduced by the restriction on the third axis direction, but there is some justification for the choice, since the data itself possesses this structure.

Although we solve a 3D problem, the discretized surface can be represented by the set of two two-dimensional arrays $v_1(s_i, r_j)$ and $v_2(s_i, r_j))$. Since our scheme is explicit in the term $F(v)$, we can consider separately the two components v_1 and v_2 at each iteration as noted in Section 2.1.2. We now present the steps of the algorithm:

1. *Addition of the expansion force.* Each boundary node along the curve at each slice is moved along vector $k_1 \overrightarrow{n}(s,r)$ where $\overrightarrow{n}(s,r)$ is the external normal to the planar curve of the slice at level r.

2. *Addition of the edge force.* At each node, we add $-k\frac{\nabla P}{\|\nabla P\|}$, where the third component of the gradient is arbitrarily set to zero to constrain the force to lie within the slice plane. The potential P is obtained from the gradient computation $\|\nabla I\|$ of the 3D image data.

3. *Smoothing.* We apply a smoothing operation by means of the matrix $(\mathcal{I} - \tau A)$ to the data V^t, separately to its components v_1^t and v_2^t. It can be verified that this matrix is banded and that the circular shifting property of the matrix in the 2D problem (see Section 2.1.2) is extended to our 3D problem. The product of a matrix of this form and the discretized surface can be viewed as the convolution of a two dimensional array with the arrays $v_1(s_i, r_j)$ and $v_2(s_i, r_j)$. Since derivatives are at most of the 4th order, this corresponds to a convolution of the discretized surface $v(ih, jk)$ by a 5×5 kernel. This smoothing can in fact be viewed as a low-pass filter. The strength of the filter is determined by the coefficients of matrix A and the time step τ.

The third step can be made faster by decomposing the convolution of the surface nodes by the 5×5 kernel into a product of two 1D low-pass filters of length 5, one in each direction, approximating the convolution kernel by a separable kernel. Although the kernel $(\mathcal{I} - \tau A)$ is not precisely a separable kernel, due to the term $w_{11}(x) \left\| \frac{\partial^2 v}{\partial r \partial s} \right\|^2$, the following procedure provides an acceptable approximation:

- *Smoothing in a cross section.* Recall that in $v_1(s, r)$ and $v_2(s, r)$, the r variable gives the slice level and s gives a spatial location along the curve. For each slice separately, the smoothing operation restricted to this slice is performed. That is, for a given slice r, the terms of the matrix $(\mathcal{I} - \tau A)$ involving data on slice r are performed. This is a first order approximation of the smoothing in the 2D problem.

- *Smoothing between cross sections.* Smoothing in the direction orthogonal to the slice planes.

Figs. 10 and 11 show example applications using a simple shape. For 20 slices of a 3D image, a white square on a black background is placed in the center of the image, to form a *frustum*: from slice to slice, the size of the square decreases and then increases again.

The 3D edge image is used to define a potential P as described in Section 2.2.3. The initial curves needed to start the process in the successive cross sections form a cylinder with a square cross-section centered on each slice whose size is smaller than that of the desired objects.

However, for the examples just described, the stack of 2D models would work just as well to find the solution. Therefore we delete from the edge image large parts of the edges in many of the cross sections (see Fig. 10). If a 2D model were applied slice-by-slice in this case, the method would close the contours, but inaccurately track the shape. Here the 3D smoothing step restores the missing parts in each slice in a coherent way from the edges in the neighboring slices, as shown in Fig. 11.

This method especially fast if the initial approximating surface is a thin tube inside the region of interest.

4 Numerical Solution by Finite Element Method (FEM)

The main problem with the 3D model is the very large number of variables, and the concomitant computation time. In the previous section, we described a simplified model, which gives satisfactory results in some cases, but generally requires further refinement. The simplified approach is only useful for tubular shapes about a single axis. To search for more general surfaces, we must solve a more complete problem, without shape constraints, except for a topological constraint defined by the boundary conditions.

As a remedy to the computational costs, we use the finite element method (FEM), which is able to effectively lower the number of discretization nodes. Initial experiments comparing a FEM and FDM in the 2D problem suggests that the FEM has a lower complexity, which becomes more important in 3D since a greater number of discretization nodes are required as compared to the 2D problem (see Section 4.3). Thus, in this section, we first present the FEM formulation of the problem in 2D, then its generalization to 3D, and then details can be found in [14].

4.1 Mathematical Formulation

We consider the evolution equation of Eqn. 3:

$$\begin{cases} \dfrac{\partial v}{\partial t} - \dfrac{\partial}{\partial s}\left(w_1 \dfrac{\partial v}{\partial s}\right) + \dfrac{\partial^2}{\partial s^2}\left(w_2 \dfrac{\partial^2 v}{\partial s^2}\right) = F\left(v\right) \\ v(s,0) = v_0(s) \quad \text{initial curve} \\ + \text{ Boundary conditions.} \end{cases} \tag{15}$$

In 3D, the equation becomes:

$$\begin{cases} \frac{\partial v}{\partial t} - \frac{\partial}{\partial s}\left(w_{10}\frac{\partial v}{\partial s}\right) - \frac{\partial}{\partial r}\left(w_{01}\frac{\partial v}{\partial r}\right) + 2\frac{\partial^2}{\partial s \partial r}\left(w_{11}\frac{\partial^2 v}{\partial s \partial r}\right) \\ + \frac{\partial^2}{\partial s^2}\left(w_{20}\frac{\partial^2 v}{\partial s^2}\right) + \frac{\partial^2}{\partial r^2}\left(w_{02}\frac{\partial^2 v}{\partial r^2}\right) = F(v) \\ v(0,s,r) = v_0(s,r) \text{ initial estimation} \\ + \text{Boundary conditions.} \end{cases} \tag{16}$$

In this case, $v = (v_1, v_2, v_3)$, and is a function of one time variable and of two spatial variables. To simplify the notation, we will consider Eqns. 15 and 16 only with zero-boundary conditions. More general cases can be handled by a simple change of variables. Moreover, as we noted in Section 2.1.2, each component of v will satisfy the same equation and may be computed separately. We thus limit in the following to the resolution of the FEM for a scalar-valued function.

In the following subsections we describe the different steps which lead to the numerical solution of the partial differential equation characterizing the deformable models.

4.1.1 Variational Problem

An approach for solving the above equations is to define the associated variational problem. The main idea can be understood by saying that the terms of Eqn. 16 are equal in some functional space if their scalar product against any vector of the space are equal. This variational problem characterizes the solution of the partial differential equations by defining the space of admissible solutions and its norm using a bilinear form $a(.,.)$ (characterizing the space norm) and a linear form $L(.)$ (characterizing the input).

In [14] we show how to define properly the bilinear form $a(.,.)$ and the linear form $L(.)$ such that solving Eqn. (1) or more generally Eqn. (8) is equivalent to solve the variational problem:

Variational Problem 1 *Find $v \in H_0^2(\Omega)$ such that:*

$$a(v,u) = L(u) \quad \forall u \in H_0^2(\Omega). \tag{17}$$

where the space $H_0^2(\Omega)$ is the Sobolev space of functions v such that $\int |D^m v|^2 < +\infty$ for $m = 0, 1, 2$ where $D^m v$ is the m^{th} order differential of function v.

The existence and uniqueness of a solution to this variational problem (17) are easily established [8], since the bilinear form $a(.,.)$ is symmetric and coercive providing $w_{kl}(s,r) > 0$.

Here, L is assumed to be independent of v. In fact, L does depend on v in our application, but in the iterative scheme, we will fix L to be constant in any given iteration (see [20] for a mathematical justification).

We give expressions for $a(.,.)$ and $L(.)$ for the 2D problem. For the 3D problem, details are provided in [14]. The bilinear form $a(.,.)$ is given by

$$a(u,v) = \int_0^1 w_1(s)u'(s)v'(s)ds + \int_0^1 w_2(s)u''(s)v''(s)ds$$

and $L = L_v$ is

$$L_v(u) = \int_0^1 F\left(v(s,t)\right) u(s)ds,$$

for the 2D case.

4.1.2 Discrete Variational Problem

A well-known approach for solving such a problem is Galerkin's method, which consists in defining a similar discrete problem, over a finite-dimensional subspace V_h of the Sobolev space $H_0^2(\Omega)$. The associated discrete problem for (17) is:

Variational Problem 2 *Find $v_h \in V_h$ such that*

$$a(v_h, u_h) = L(u_h) \quad \forall \ u_h \in V_h. \tag{18}$$

A solution v_h of this discrete problem is an approximation of the solution v of the continuous variational problem.

This discrete problem leads to a finite linear system defined over the finite-dimensional space V_h.

The FEM provides an efficient tool for defining the space V_h.

4.1.3 The Finite Element Method

The finite element method is characterized by three aspects in the construction of the space V_h:

(FEM1) A tessellation is established over the parametrization set $\Omega = [0,1]$ ($[0,1] \times [0,1]$ in 3D);

(FEM2) The functions $v_h \in V_h$ are typically piecewise polynomial; and

(FEM3) The basis of functions for the space V_h are chosen such that they have small support.

Hence, the FEM provides a finite dimensional space V_h and a discrete representation of the solution v_h approximating the solution v of the variational problem (17).

We use a conform finite element method which insures that the space V_h is a subspace of $H_0^2(\Omega)$ and that the basis functions are $\mathcal{C}^1$ continuous. In the following we describe the choice of the subspace V_h in the 2D and 3D case.

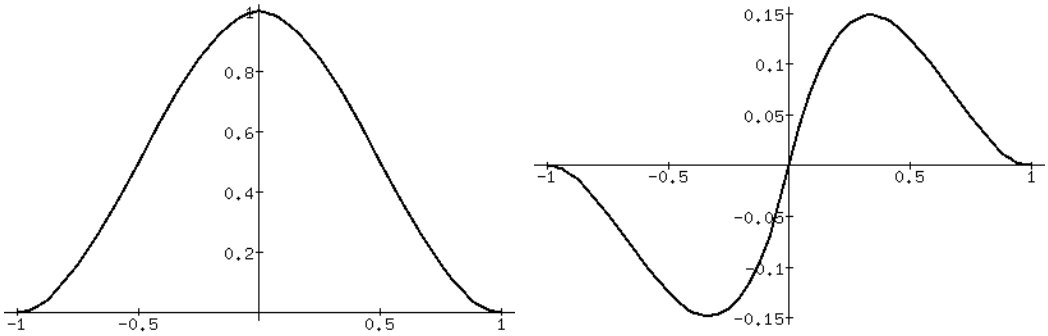

Figure 2: Plots of the two basis functions ϕ and Ψ for the 2D FEM.

4.1.4 The 2D Curve Case

We consider a uniform subdivision of $\Omega = [0,1] = \bigcup_{i=1}^{N}[ih,(i+1)h]$, where N is the number of discretization points and $h = \dfrac{1}{N+1}$.

Since the variational problem 17 uses the space of admissible functions $H_0^2([0,1])$, the space V_h must satisfies $V_h \subset \mathcal{C}^1 \cap H_0^2([0,1])$ (for details see [8]). A choice for the subspace V_h is defined by:

$$V_h = \left\{ v \in \mathcal{C}^1\left([0,1]\right),\ v_{|[x_i,x_{i+1}]} \in P_3([x_i,x_{i+1}])\ \ 0 \leq i \leq N \right\}$$

where $P_k(I)$ is the vector space of polynomials of degree k or less, restricted to the interval $I \subset R$. We use the notation $v_{|I}$ to mean the restriction of the function v to the subset I. The space P_3 has been chosen since a polynomial $p \in P_3$ is uniquely determined by its values and the values of its first derivative at two distincts points. The basis functions of V_h are ϕ_i and Ψ_i, $1 \leq i \leq N$ defined by:

$$\phi_i(x_j) = \delta_{ij}, \quad \phi_i^{'}(x_j) = 0 \ \ 1 \leq j \leq N \tag{19}$$

$$\Psi_i(x_j) = 0, \quad \Psi_i^{'}(x_j) = \delta_{ij} \ \ 1 \leq j \leq N \tag{20}$$

where:

$$\delta_{ij} = \begin{cases} 1 & \text{if } i = j \\ 0 & \text{otherwise.} \end{cases}$$

Analytic expressions for the ϕ_i and Ψ_i are given in [14]; Fig. 2 shows plots of the functions.

A function $v_h \in V_h$ is completely defined by the values of v_h and v_h' at each of the nodes x_i, and we have the identity:

$$v_h = \sum_{i=1}^{N} v_h(x_i)\phi_i + \sum_{i=1}^{N} v_h^{'}(x_i)\Psi_i, \tag{21}$$

yielding an expression for v_h in terms of a finite collection of unknowns.

Using the FEM and the above choices for the implementation in order to compute the solution to the 2D balloon model, we obtain the results presented in Figs. 14 and 15.

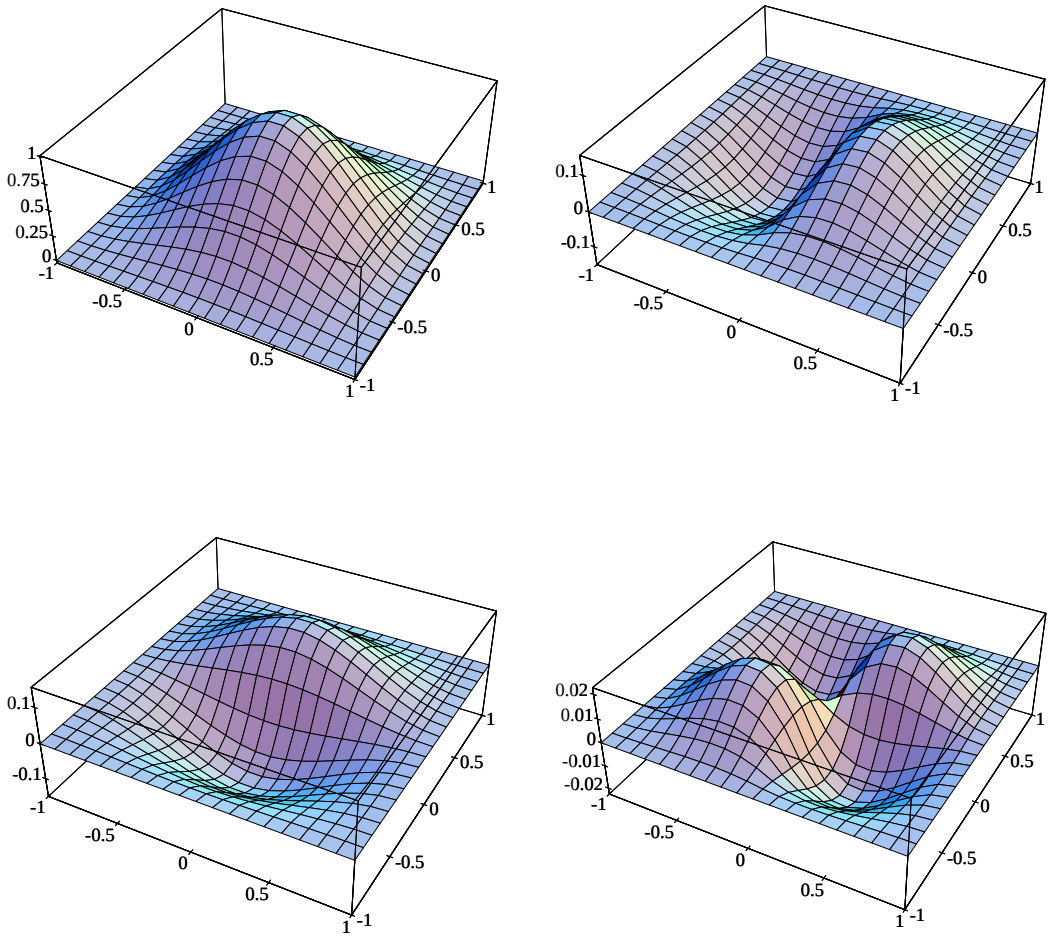

Figure 3: Surface plots of the four basis functions φ, ψ, η and ζ for the 3D FEM

4.1.5 The 3D Surface Case

A tessellation of the domain Ω in 3D and the construction of the subspace V_h using the Bogner-Fox-Schmit (BFS) elements are given in [14] In this space, a function is completely determined by four values at each nodal point $a_{ij} = (ih_s, jh_r)$, specifically, the values for v_h, $\frac{\partial v_h}{\partial s}$, $\frac{\partial v_h}{\partial r}$ and $\frac{\partial^2 v_h}{\partial s \partial r}$. The corresponding basis functions are shown in Fig. 3. These basis functions can also be obtained through a tensorial product of the functions ϕ and Ψ (19-20).

The tesselation of the domain Ω could be done with triangular patches providing an adaptive mesh and requiring a bigger computational complexity (see [8] for a complete description of the different basis functions). The choice of the BFS elements is due to their ability to tesselate easily rectangular domains and mainly to the reduced number of

neighboring nodes and degrees of freedom (four at each nodal point).

Expressing $v_h \in V_h$ in the BFS basis leads to the identity:

$$v_h = \sum_{i,j=0}^{N_s-1,N_r-1} v_h(a_{ij})\varphi_{ij} + \frac{\partial v_h}{\partial s}(a_{ij})\psi_{ij} + \frac{\partial v_h}{\partial r}(a_{ij})\eta_{ij} + \frac{\partial^2 v_h}{\partial s \partial r}(a_{ij})\zeta_{ij}, \tag{22}$$

which provides a $\mathcal{C}^1$ function defined over the set Ω depending on a finite collection of parameters.

4.2 Discretization of the Problem

Once the space is discretized and the function v is represented as an element in a finite dimensional subspace, a linear system results:

$$A \cdot V = L, \tag{23}$$

where the matrix A is symmetric, positive definite and heptadiagonal (tridiagonal per bloc in the 3D case) and V is the vector of coordinates of v_h in the chosen basis. These coordinates are in fact the values of v_h and its derivatives $\frac{\partial v_h}{\partial s}$, $\frac{\partial v_h}{\partial r}$, and $\frac{\partial^2 v_h}{\partial s \partial r}$ at the nodes of the tessellation.

Having discretized the problem 15 in space, we next have to discretize its variational formulation:
given $v_0 \in L^2(\Omega)$ and $F \in L^2(0,T,L^2(\Omega))$,
find a function $v \in L^2(0,T,H_0^2(\Omega)) \cap \mathcal{C}^1(0,T,L^2(\Omega))$ satisfying:

$$\begin{cases} \frac{d}{dt}(v(t),\psi) + a(v(t),\psi) = L_v(\psi)\ \forall \psi \in H_0^2(\Omega) \\ v(0) = v_0 \\ w_1(s), w_2(s) \in L^\infty(\Omega), \quad w_1(s) \text{ and } w_2(s) \geq \alpha > 0 \end{cases} \tag{24}$$

We then use finite differences in time. Finite differences in time may be viewed as as a way to formulate the following iterative method. We are only interested in the final result and so do not need an accurate solution in time. The result is simply:

$$\begin{cases} \frac{V^t - V^{t-1}}{\tau} + A \cdot V^t = L_{V^{t-1}} \\ V^0 = v_0 \text{ initial estimation.} \end{cases} \tag{25}$$

where τ is the time step. Eqn. 25 can be written in a form similar to the finite differences formulation (4), yielding

$$(\mathcal{I} + \tau A) \cdot V^t = V^{t-1} + \tau L_{V^{t-1}}, \tag{26}$$

which is the discrete version of Eqn. 16. To solve the linear system $M \cdot V = N$ at each time step, for which the matrix $M = (\mathcal{I} + \tau A)$ is banded, symmetric and positive definite,

we first note that M does not depend on t, and so its inverse may be precomputed using a Cholesky factorization.

Note that we assume here that the coefficient functions w_{ij} remain constant in time. If the coefficients do change in time, or even if they do not, an alternative method to solve this linear system is by means of a Conjugate Gradient method, in which the solution V^{t-1} is taken as an initial guess at time t. This approach appears to have a faster convergence than the Cholesky factorization method.

Remark that when using the FEM, the solution is less sensitive than with FDM to deformations of the mesh. It permits apparition of larger distances between neighboring nodes which happen, for example, when using the balloon model. However, like with the FDM, we periodically reparametrize the curve or surface, but without adding new node points. For a curve in 2D, we construct a new parametrization using the existing curve by sampling at a regular distance between nodes, with a given number of nodes. For a surface in 3D, we do the same as in 2D in both directions of the parametrization, one direction after the other.

4.3 Performance and Complexity Analysis

The better complexity of the FEM was studied in 2D and guided us to use it for the 3D generalization of the model.

The FEM has a better complexity because, as compared to the FDM, the step size of the spatial discretization can be larger with the FEM, resulting in linear systems of smaller size. In general, we observe with the 2D FDM model with our application that:

- If the step size is more than 2 pixels, then the curves passes over the edges or fails to be attracted to edges;
- For the balloon model, a dynamic reparametrization is often required since the length of the curve increases significantly during the time steps; and
- The size of the linear system is of the order of the length of the curve, due to the reparametrization.

While for the FDM, we follow the evolution of a set of points, with finite elements for the 2D model, the curve which is between two points of the grid can deform, so that the image forces between two points are also considered. The computation of vector L (see section 4.5) is made by numerical integration, interpolating along the interval $[(i-1)h, (i+1)h]$ for each node $s_i = ih$ of the subdivision. The numerical integration is made at the pixel size so that no information is lost.

If we compare results of FEM with those obtained using a finite difference method (FDM) (as in [12]), we find out that, as expected, the finite element method requires fewer points for the curve discretization and gives more stable results. This FEM gives also a faster convergence to an equilibrium.

Since the methods lead to the linear systems (25) for FEM or (4) for FDM, the algorithmic complexity can be deduced by examining the associated linear systems.

Let N be the number of the discretization points along the interval $[0, 1]$. For the FEM, the matrix A is a $2N \times 2N$ heptadiagonal array, while it is only $N \times N$ pentadiagonal for the FDM. In the FDM approach, the number of points N must be at least equal to the length l, in pixels, of the initial guess, and may have to increase in size. On the other hand, for the finite element method, the number of points N is typically of the order of $l/6$. Thus the matrix size for the FEM case is $\frac{2l}{6}$ by $\frac{2l}{6}$, which is 9 times smaller than with the FDM.

Moreover, with the FEM, the same number of nodes in the system is held fixed for all iterations. An initial computation of the inverse of the matrix A is sufficient for the whole process.

4.4 Elasticity and Rigidity Coefficients

The elasticity and rigidity coefficients w_{kl} play an important role in the convergence process of the surface toward the image edges. These coefficients must be chosen in a correct way such that the internal forces generated by terms of the energy E comprising the coefficients w_{kl} have the same magnitude as the external forces generated by the potential $P(v)$. Since a minimum of the energy E will involve a trade-off between the internal and external energy, the solution surface should fit the edge points while being smooth and regular. If the internal energy is preponderant, then the surface will tend to collapse on itself without detecting image edges, whereas if the external energy predominates, then the surface will converge along the image edge without any degree of smoothing.

To insure that both internal and external energy have the same order of magnitude, we have found it sufficient to choose the coefficients w_{kl} such that the linear system of Eqn. 16 is well-conditioned. For example, the following assignments result in a well-conditioned system:

$$w_{10} = w_{01} = h_s^2 h_r^2 \quad \text{and} \quad w_{20} = w_{11} = w_{02} = h_s^3 h_r^3,$$

where h_s and h_r are the discretization step of Ω. Setting $w_{10} = w_{01}$ and $w_{20} = w_{11} = w_{02}$ presupposes that the 3D image data is isotropic, and thus that all directions have equal weight.

In [9], we propose a general approach for determining the regularizing parameters w_{ij} given an error margin on the accuracy of the reconstructed surface. This method allows also surface reconstruction preserving discontinuities.

4.5 The Computation of the Vector L

The computation of $L = (L(e_1), \ldots, L(e_N)))^T$ (where e_p is the chosen basis of V_h) depends upon $P = -\|\nabla I(x,y)\|^2$ which is known only at pixel (or voxel in 3D) locations. The integrals $L(e_l) = \int_\Omega F\left(v^{t-1}(s,r)\right) e_l(s,r)\, dsdr$ represents the contribution of the external forces which cause the surface to be attracted toward the edges, and contribute to the linear system that we must solve at each iteration. Thus, the more we weight the potential $P = -\|\nabla I\|^2$, the more closely the result tracks the edges and the faster is the convergence (at the expense of smoothness).

Since the potential P is known only at pixel locations, we must compute the $L(e_l)$ with a numerical integration. Consequently we compute ∇P at interpolated points $(x,y,z) \in \mathbb{R}^3$ by a trilinear interpolation of the eight neighbors.

To take into account all the contributions of the external forces, we modified the numerical integration formula such that every image point in the set $v([(i-1)h_s, (i+1)h_s] \times [(j-1)h_r, (j+1)h_r])$ is involved in the computation of each term $L(e_p)$. This method allows us to do an "adaptive subdivision" of the rectangle $K_{ij} = [ih_s, (i+1)h_s] \times [jh_r, (j+1)h_r]$ without adding nodal points and, consequently, without increasing the size of the linear system to be solved. This method significantly reduces the algorithmic complexity while increasing the accuracy and the convergence speed.

5 3D Results

Using a real 3D deformable model to segment a 3D image provides better results than the iterated application of a 2D deformable model to successive 2D cross-sections. In effect, the 3D model easily bridges edge gaps in 3D, i.e., not only within a cross section, but also between cross-sections, insuring that the result is globally a smooth surface.

Compared to the simplified approaches of Section 3, the use of the full 3D model to segment 3D data significantly improves the robustness of the segmentation; for instance it is even possible to remove all the edges of a single cross section (assuming that the edges are correctly detected in other slices) without seriously degrading the final result. Fig. 16 shows the 3D reconstruction obtained by using the 3D balloon model of section 3 applied to the data of Fig. 10. The final surface is more accurate and smoother than that obtained with the simplified approach shown in Fig. 11. On a Sun Sparc station, the

result shown in Fig. 16 takes however about ten times more computation time than that required for the simplified approach.

Figs. 17 and 18 demonstrate another example of the 3D model applied to artificial data. In this case, the initial surface is a cylinder (Fig. 17), where we have removed some edges in three successives cross sections, for comparison purposes. The deformable surface restores the missing edges and obtains a perfect reconstruction of the cylinder (Fig. 18), whereas a 2D model fails due to the missing edges, even if we use the same attraction force as for the 3D model.

Fig. 18 and also Figs. 22 and 23 show cross sections of the original 3D image overlaid with the reconstructed surface on the same plane.

For our final example, we use real data: image data of a part of a human head obtained with Magnetic Resonance Imaging (MRI). We make use of the "weight force" described in Section 2.2.2, which allows us to begin with a much simpler initial surface than in [10]; In this case, the initial surface is a plane placed on one side of the 3D image. The weight force makes the surface fall through the image until it is caught progressively by the shape of the face. The evolution of the surface is shown in Figs. 19, 20 and 21. The final result is obtained after about 100 iterations. We show the final result overlaid on the original image data in vertical (Fig. 22) and horizontal (Fig. 23) cross sections. Here, by vertical and horizontal slices, we mean with respect to the representation of Fig. 21. We remark the accurate localization by the surface of the 3D edges.

6 Conclusion

One of the goals of the regularization process in surface reconstruction is to obtain good estimates of partial derivatives of the surface in order to compute differential characteristics. Since the result of the deformable model reconstruction described here is an analytical description of class $\mathcal{C}^\infty$ almost everywhere (except along the borders of the finite elements, where the representation is only of class $\mathcal{C}^1$), we may compute, for example the first and second fundamental forms of the surface [18]. We could then extract a curvature-based primal sketch of the surface [6, 26], including intrinsic features such as parabolic lines, extrema of curvatures, and umbilic points, which can be used as landmarks for 3D image interpretation [2]. We are conducting such a program [10], and will present results in a subsequent paper.

Another goal of this representation is the elastic matching of extracted features to an atlas, which is also the problem discussed in [3]. For this purpose, we would deform a curve or surface to best match the pattern using some measure of the distortion, such as the area between the two curves. This was also studied in [35] with simple geometric

shapes as templates which are deformed to match the image.

In order to achieve a representation on a deformable model, we have presented a 3D generalization of the balloon model introduced in [12] which solves some of the problems encountered with the "snake" model of [23, 32]. We began with a survey of the use of an attraction potential generated by available edge data to reconstruct a curve or surface. We demonstrated some properties of deformable surfaces and their interaction with 3D edge points. Our approach here extends an earlier approach, reported in [12], where we use a series of 2D contours in successive cross sections to make a 3D reconstruction of the surface of the ventricles. The simplified approach given here was implemented by defining a 3D surface as a series of 2D planar curves making a simultaneous and interdependent evolution, using the Eqn. 9. The solution method used a finite difference approach and an explicit scheme, which produced a fast computational algorithm.

We then implemented a Finite Element Method solution strategy, to solve the full 3D problem. The reason for choosing a FEM approach as opposed to a Finite Difference Method was that:

1. The FEM approach requires fewer discretization points and consequently produces a smaller linear system to solve, thus reducing significantly the algorithmic complexity;

2. The FEM approach produces more accurate results, since the external forces can be computed more accurately;

3. The FEM approach provides an analytical representation of the surface.

To solve the full 3D model of surface, we used a Bogner-Fox-Schmit finite rectangular element.

This method has been tested for several applications in medical image analysis. We showed promising results of our model on MR (magnetic resonance) images, to extract features like the contour of a face.

References

[1] N. Ayache, J.D. Boissonnat, E. Brunet, L. Cohen, J.P. Chièze, B. Geiger, O. Monga, J.M. Rocchisani, and P. Sander. Building highly structured volume representations in 3D medical images. In *Computer Aided Radiology*, Juin 1989. Berlin, West-Germany.

[2] N. Ayache, J.D. Boissonnat, L. Cohen, B. Geiger, O. Monga, J. Levy-Vehel, and P. Sander. Steps toward the automatic interpretation of 3D images. *NATO ASI Series on 3D Imaging in Medicine*, F 60:107–120, 1990.

[3] Ruzena Bajcsy and Stane Kovacic. Multiresolution elastic matching. *Computer Vision, Graphics, and Image Processing*, 46:1–21, 1989.

[4] Andrew Blake and Andrew Zisserman. *Visual Reconstruction*. The MIT Press, 1987.

[5] Gunilla Borgefors. Distance transformations in arbitrary dimensions. *Computer Vision, Graphics, and Image Processing*, 27:321–345, 1984.

[6] Michael Brady, Jean Ponce, Alan Yuille, and Haruo Asada. Describing surfaces. In Hideo Hanafusa and Hirochika Inoue, editors, *Proceedings of the Second International Symposium on Robotics Research*, pages 5–16, Cambridge, Mass., 1985. MIT Press.

[7] John Canny. A computational approach to edge detection. *IEEE Transactions on Pattern Analysis and Machine Intelligence*, PAMI-8(6):679–698, November 1986.

[8] P. G. Ciarlet. *The finite element methods for elliptic problems*. NORTH-HOLLAND, 1987.

[9] Isaac Cohen. *Modèles déformables 2-D et 3-D: Application à la segmentation d' images médicales*. PhD thesis, Université Paris-IX Dauphine, June 1992.

[10] Isaac Cohen, Laurent D. Cohen, and Nicholas Ayache. Using deformable surface to segment 3-D images and infer differential structures. In *Proc. Second European Conference on Computer Vision*, pages 648–652, Santa Margherita Ligure, Italy, May 1992.

[11] Laurent D. Cohen. On active contours models. In *Proceedings of NATO ASI Active perception and Robot vision*, Maratea, July 1989. Springer.

[12] Laurent D. Cohen. On active contour models and balloons. *Computer Vision, Graphics, and Image Processing : Image Understanding*, 53(2):211–218, March 1991.

[13] Laurent D. Cohen and Isaac Cohen. A finite element method applied to new active contour models and 3D reconstruction from cross sections. In *Proc. Third International Conference on Computer Vision*, pages 587–591, Osaka, Japan, December 1990.

[14] Laurent D. Cohen and Isaac Cohen. Finite element methods for active contour models and balloons from 2D to 3D. Technical Report 9124, Ceremade, December 1991.

[15] P. E. Danielsson. Euclidean distance mapping. *Computer Vision, Graphics, and Image Processing*, 14:227–248, 1980.

[16] H. Delingette, M. Hebert, and K. Ikeuchi. Shape representation and image segmentation using deformable surfaces. In *Proc. 1991 IEEE Computer Society Conference on Computer Vision and Pattern Recognition*, Maui, Hawai, June 1991.

[17] Rachid Deriche. Using canny's criteria to derive a recursively implemented optimal edge detector. *International Journal of Computer Vision*, pages 167–187, 1987.

[18] Manfredo P. do Carmo. *Differential Geometry of Curves and Surfaces*. Prentice-Hall, Englewood Cliffs, 1976.

[19] Pascal Fua and Yvan G. Leclerc. Model driven edge detection. In *DARPA Image Understanding Workshop*, 1988.

[20] R. Glowinski. *Numerical Methods for Nonlinear Variational Problems*. Springer-Verlag, 1984.

[21] W.E.L. Grimson. *From Images to Surfaces: A computational study of the Human Early vision system*. The MIT Press, 1981.

[22] I.L. Herlin and N. Ayache. Features extraction and analysis methods for sequences of ultrasound images. In *Proceedings of the Second European Conference on Computer Vision 1992*, Santa Margherita Ligure, Italy, May 1992.

[23] Michael Kass, Andrew Witkin, and Demetri Terzopoulos. Snakes: Active contour models. *International Journal of Computer Vision*, 1:321–331, 1987.

[24] O. Monga and R. Deriche. 3D edge detection using recursive filtering. application to scanner images. In *IEEE Computer Society Conference on Vision and Pattern Recognition*, San Diego, June 1989.

[25] T. Poggio, H. Voohrees, and A. Yuille. A regularized solution to edge detection. Technical Report A.I. Memo 833, MIT, May 1985.

[26] Jean Ponce and Michael Brady. Toward a surface primal sketch. In *Proceedings, IJCAI*, 1985.

[27] Demetri Terzopoulos. Image analysis using multigrid relaxation methods. *IEEE Transactions on Pattern Analysis and Machine Intelligence*, PAMI-8(2):129–139, March 1986.

[28] Demetri Terzopoulos. Regularisation of inverse visual problems involving discontinuities. *IEEE Transactions on Pattern Analysis and Machine Intelligence*, PAMI-8(4):413–424, July 1986.

[29] Demetri Terzopoulos. On matching deformable models to images. In *Topical meeting on machine vision, Technical Digest Series*, volume 12, pages 160–163. Optical Society of America, 1987.

[30] Demetri Terzopoulos. The computation of visible-surface representations. *IEEE Transactions on Pattern Analysis and Machine Intelligence*, PAMI-10(4):417–438, July 1988.

[31] Demetri Terzopoulos, Andrew Witkin, and Michael Kass. Symmetry-seeking models for 3D object reconstruction. *International Journal of Computer Vision*, 1(3):211–221, October 1987.

[32] Demetri Terzopoulos, Andrew Witkin, and Michael Kass. Constraints on deformable models: recovering 3D shape and nonrigid motion. *AI Journal*, 36:91–123, 1988.

[33] A.N. Tikhonov and V.Y. Arsenin. *Solutions of ill-posed problems*. Winston and sons, 1977.

[34] Isaac Weiss. Shape reconstruction on a varying mesh. *IEEE Transactions on Pattern Analysis and Machine Intelligence*, PAMI-12(4), April 1990.

[35] A.L. Yuille, D.S. Cohen, and P.W. Hallinan. Feature extraction from faces using deformable templates. In *Proceedings of Computer Vision and Pattern Recognition*, San Diego, June 1989.

[36] S.W. Zucker and R.M. Hummel. A three-dimensional edge operator. *IEEE Transactions on Pattern Analysis and Machine Intelligence*, PAMI-3(3):324–331, May 1981.

7 Figures

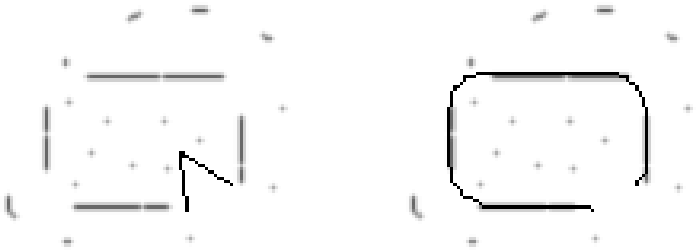

Figure 4: Advantage of the balloon model: the initial curve (in black, on the left) neither collapses nor gets trapped by spurious isolated edges points. It robustly converges toward the desired rectangle shape (on the right). The background image is the attraction potential generated by hand-drawn contours (see next figure).

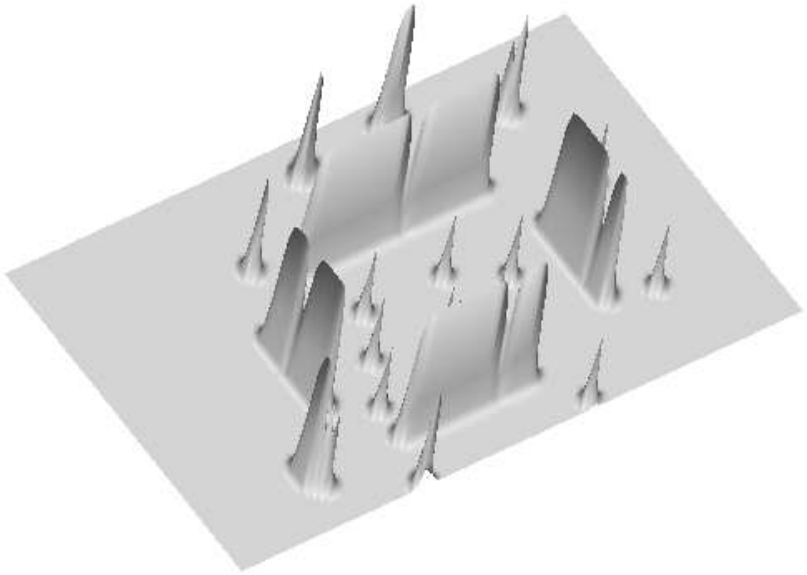

Figure 5: Attraction potential surface generated by convolution of a Gaussian and the edge contours defined by hand shown in Fig. 4. The surface is shown upside down for sake of clarity. The curve is attracted to minima of the potential, which are maxima as seen in the figure. The potential around isolated points shows the shape of the Gaussian used. The attraction force is small outside a neighborhood of an edge point.

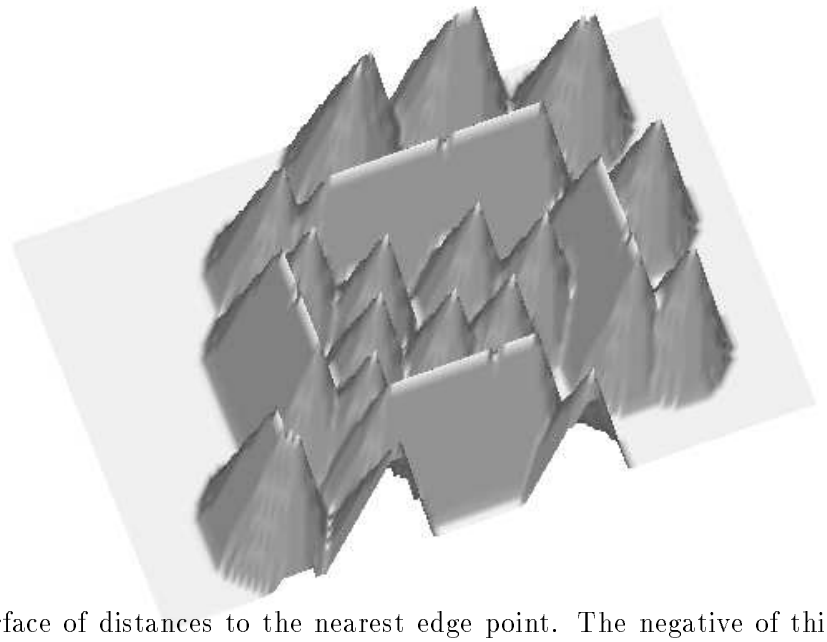

Figure 6: Surface of distances to the nearest edge point. The negative of this surface, as the previous one, may be used as a potential.

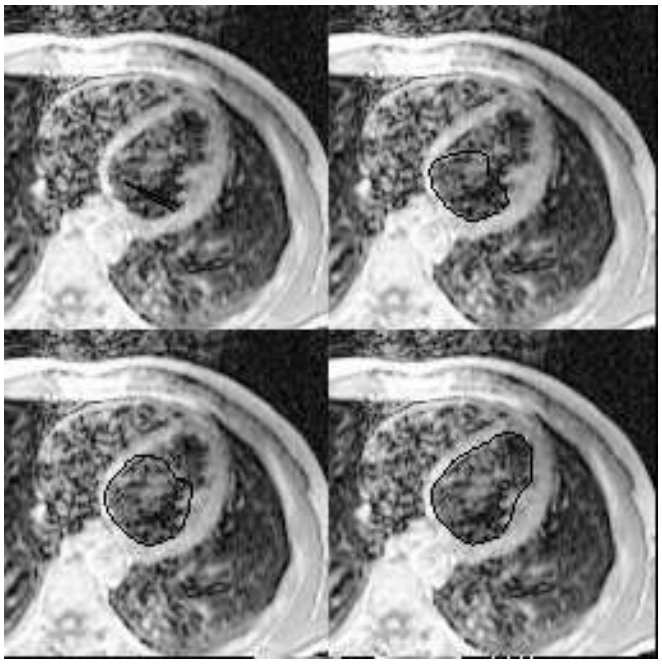

Figure 7: An MRI image. Evolution of the balloon curve to detect the left ventricle. Here we give illustration of the robustness of the balloon model: the final result can be achieved from almost any initial curve given within the interior of the ventricle (see also Figs. 14 and 15).

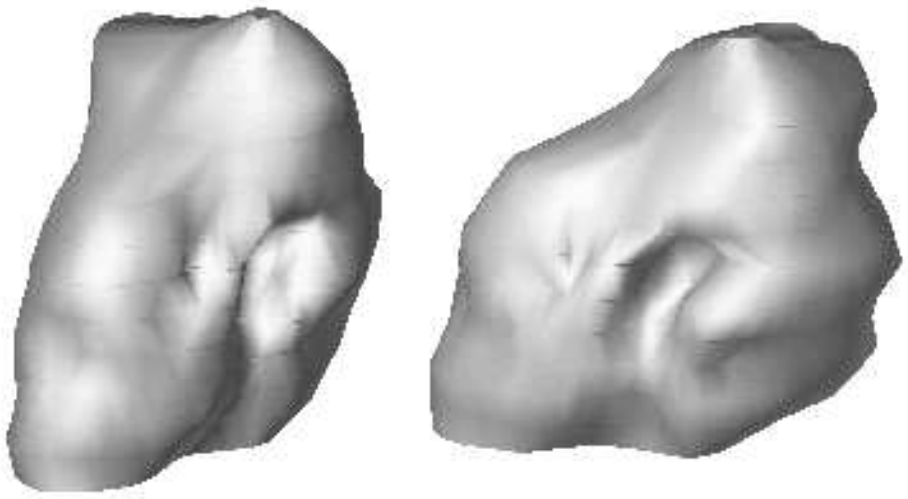

Figure 8: 3D reconstruction from a sequence of 2D contour models: two views of the reconstructed inside cavity of the left ventricle.

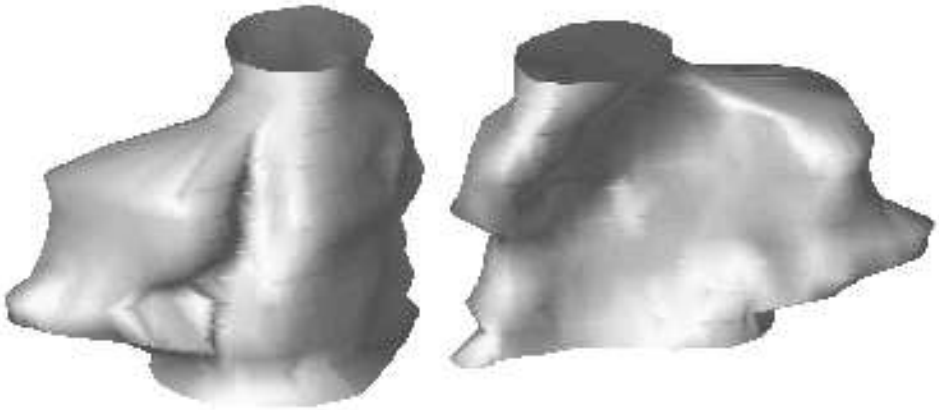

Figure 9: 3D reconstruction from a sequence of 2D contour models: two views of the reconstructed inside cavity of the right ventricle.

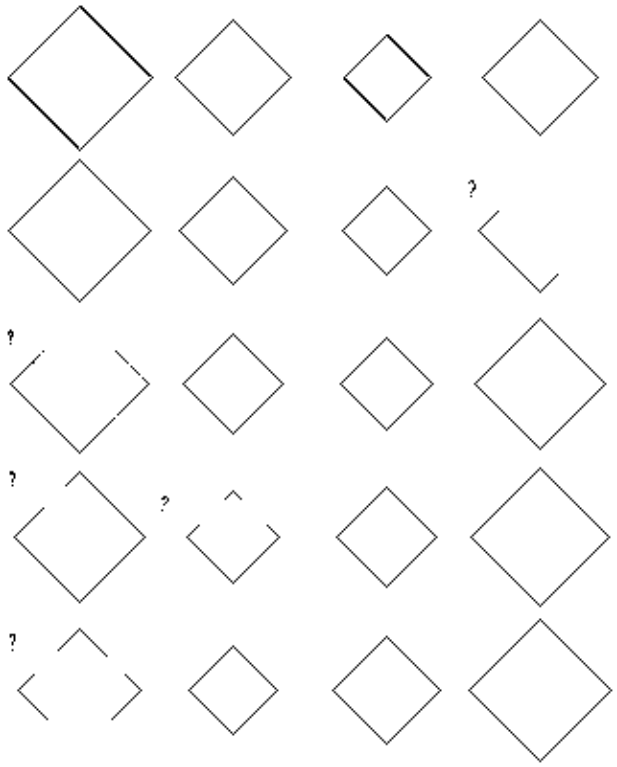

Figure 10: Edge image of the frustum after erasing some parts. The cross sections with a "?" were modified. The sequence of cross sections is ordered from top to bottom and from left to right. The square shrinks to an intermediate size, and then increases back to the original size.

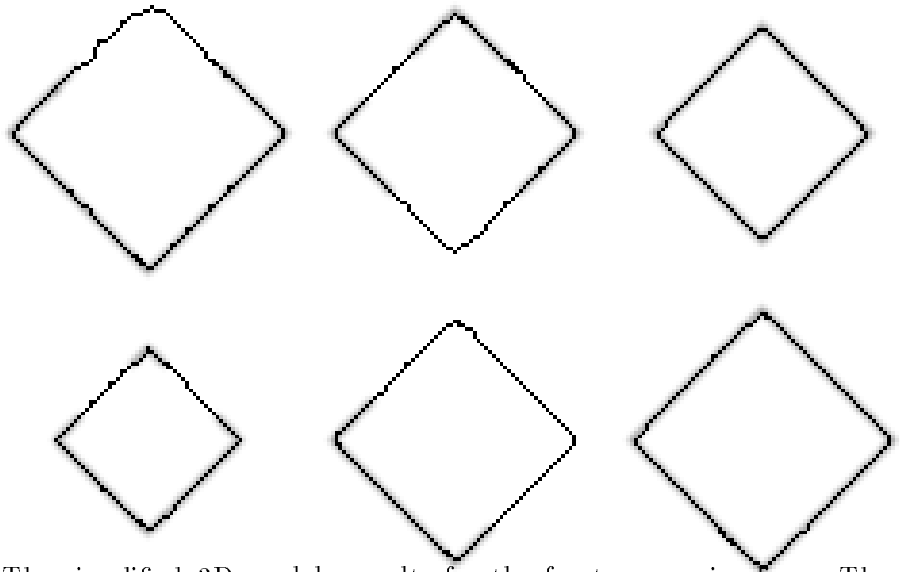

Figure 11: The simplified 3D model: results for the frustum on six slices. They are ordered from left to right and from top to bottom. The two cross sections on the far right correspond to complete contours, the other ones had some parts erased.

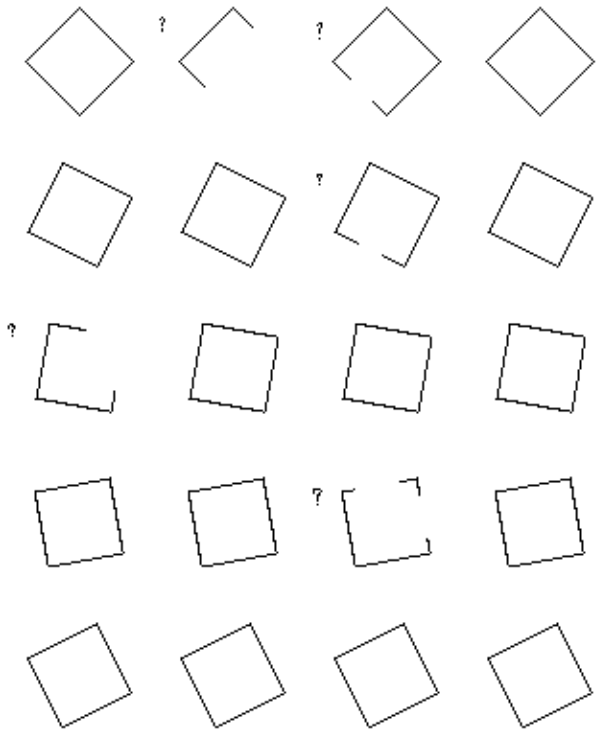

Figure 12: Contours of the bended tube after erasing some parts. The sequence of cross sections is ordered from top to bottom and from left to right. The square, always of the same size, rotates with a constant angle from a slice to the next.

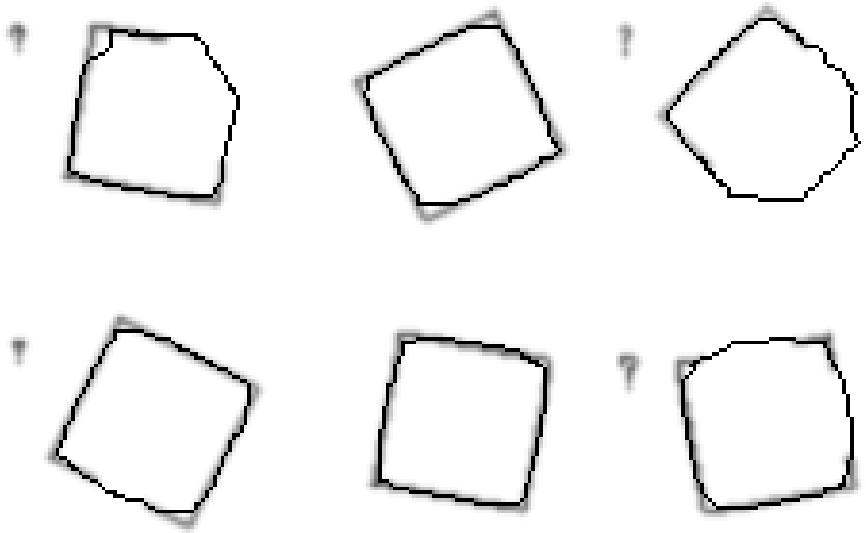

Figure 13: The simplified 3D model: results for the bended tube on six slices. They are ordered from left to right and from top to bottom. The cross sections with a "?" had some parts erased. The second follows the first, the three bottom slices are also successive.

Figure 14: Using the FEM. Evolution (from left to right) of the balloon curve to detect the left ventricle (see also next figure).

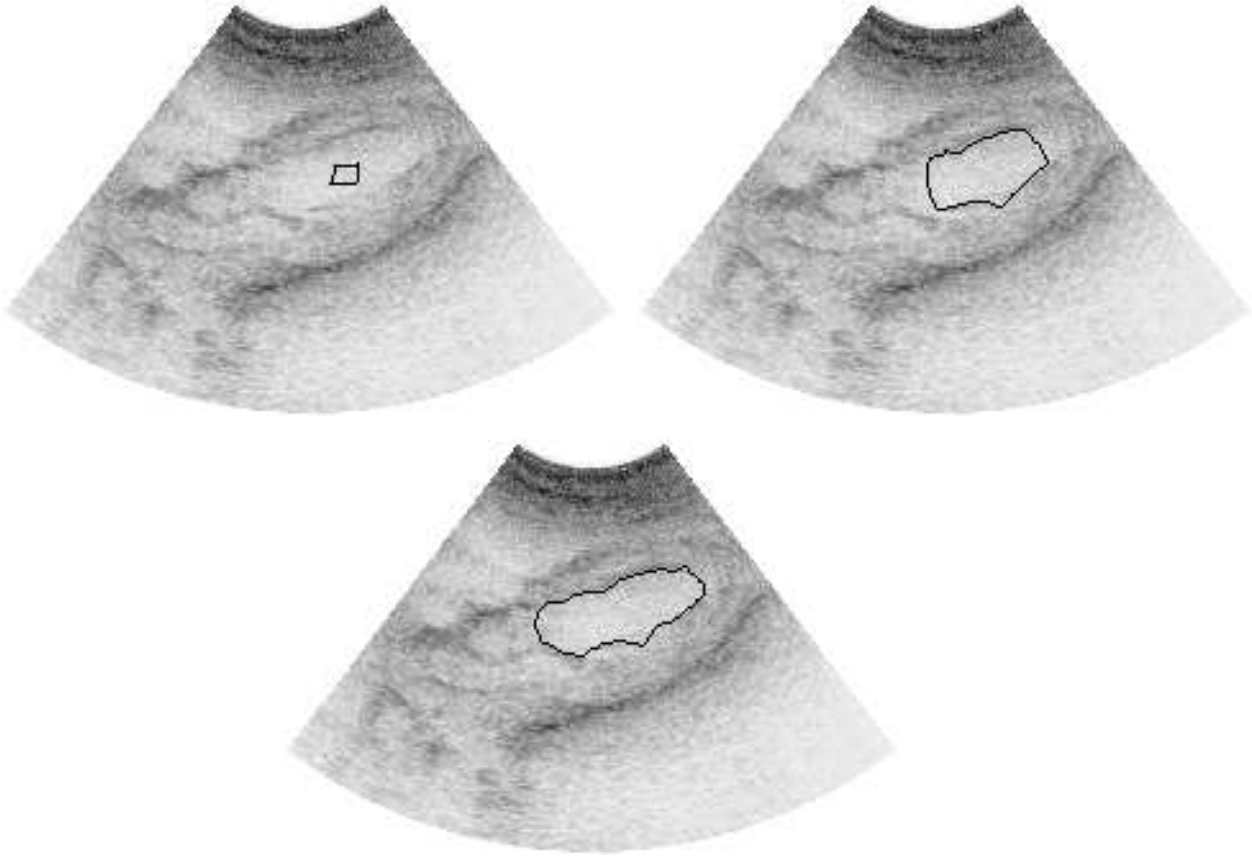

Figure 15: Using the FEM on echographic images.

Figure 16: Representation of the 3D reconstructed surface using the data of Fig. 10.

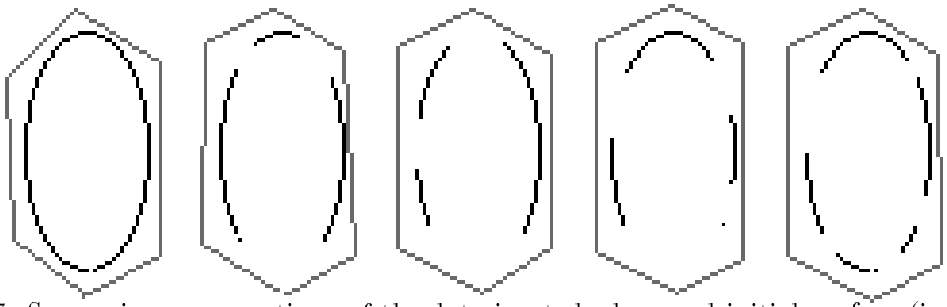

Figure 17: Successive cross sections of the deteriorated edges and initial surface (in grey) given by the user.

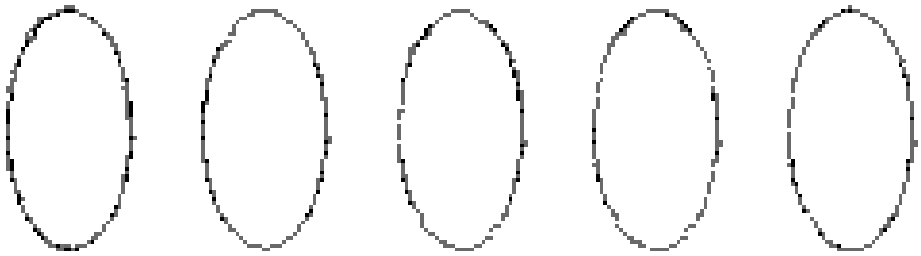

Figure 18: Here we show how the deformable surface (in grey) can reconstruct deteriorated edges by maintaining 3D homogeneity. In this example, a 2D model cannot reconstruct the missing edges even if we use a 3D potential.

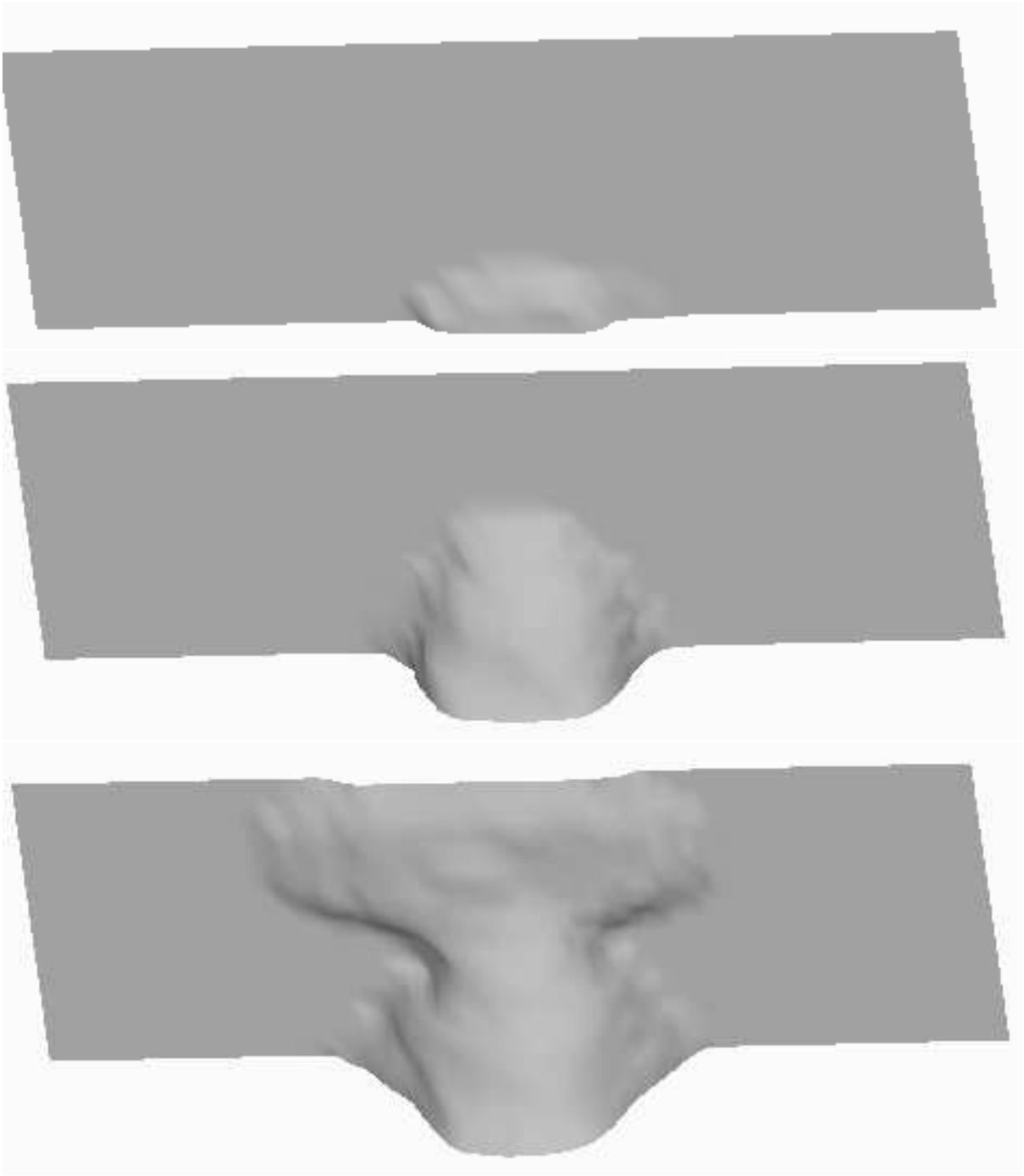

Figure 19: Evolution of the 3D surface "falling" on a 3D MRI image of a head. The initial surface is a plane on the border of the image.

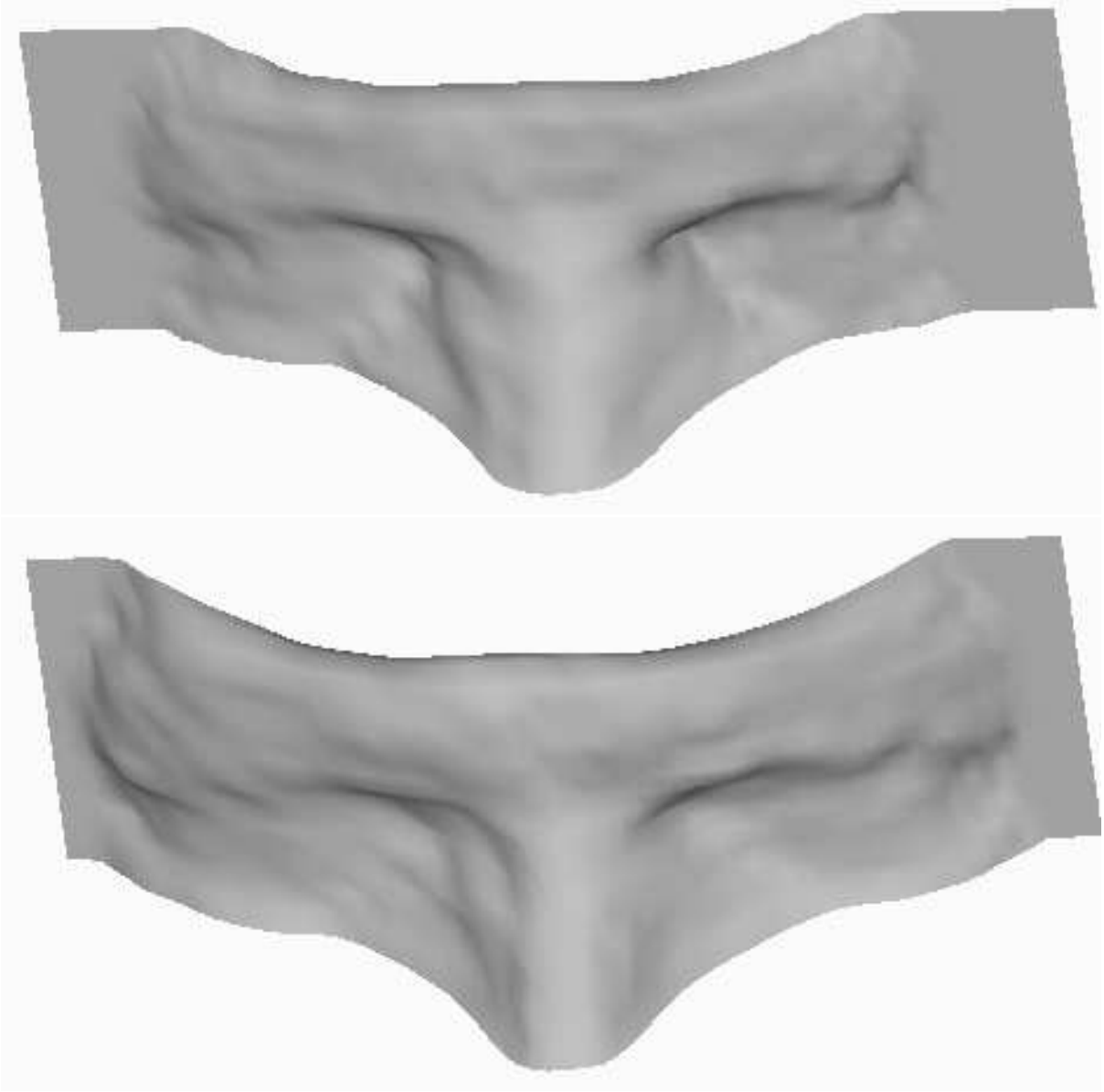

Figure 20: Evolution of the 3D surface continued.

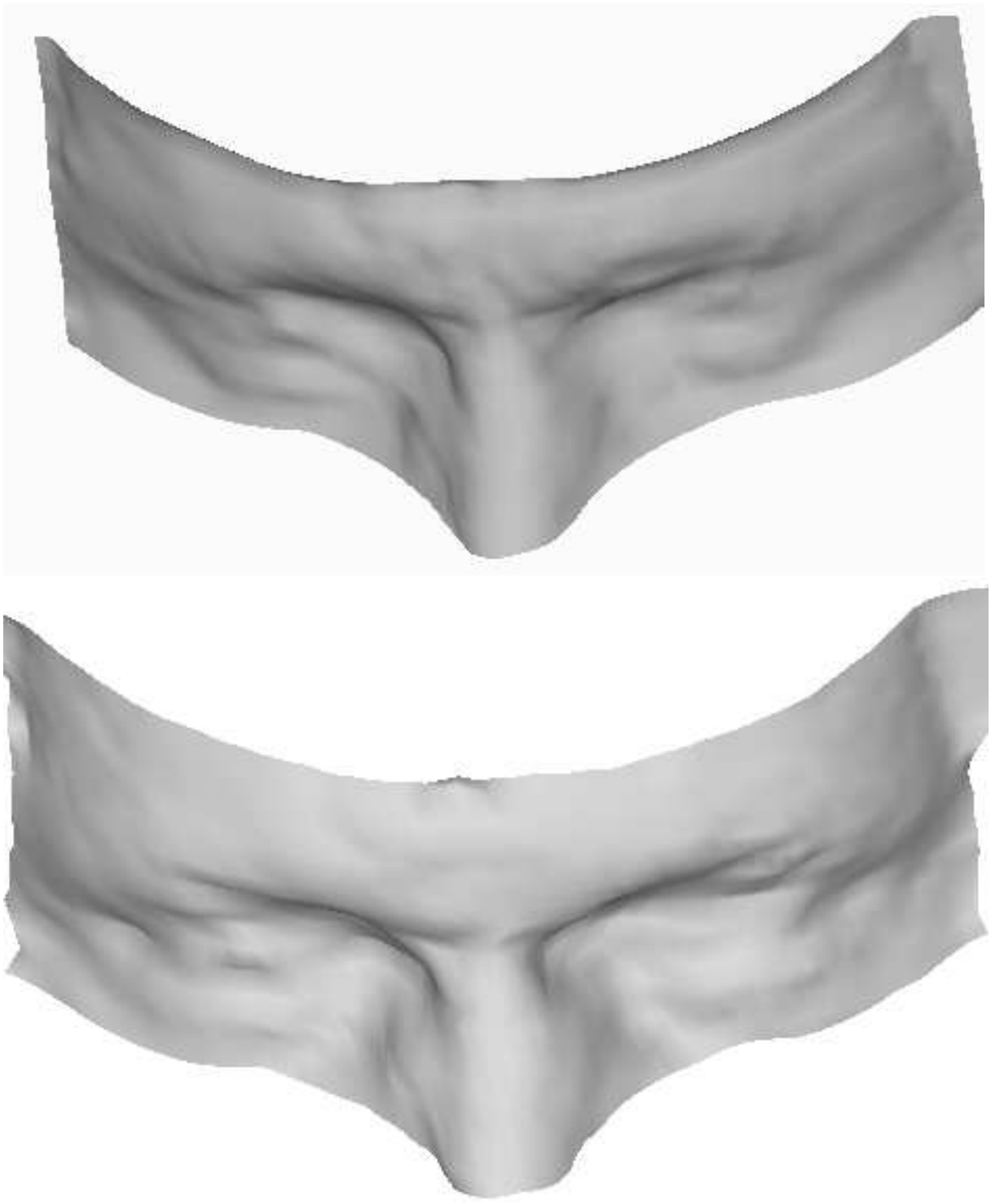

Figure 21: Final result of the face.

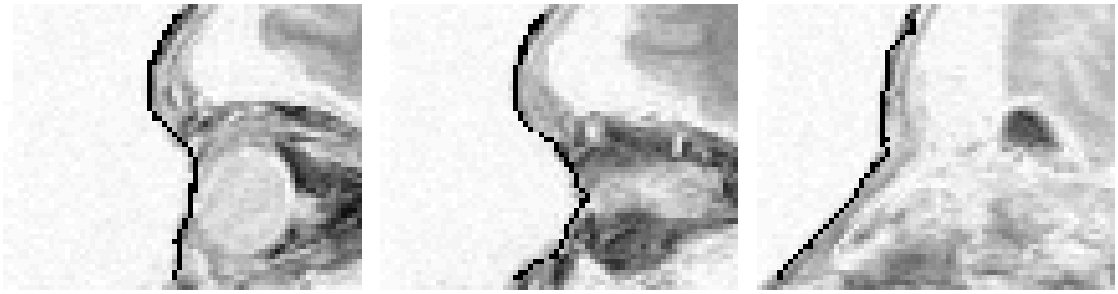

Figure 22: Overlays of some vertical cross sections of the final surface obtained by the algorithm with the original data.

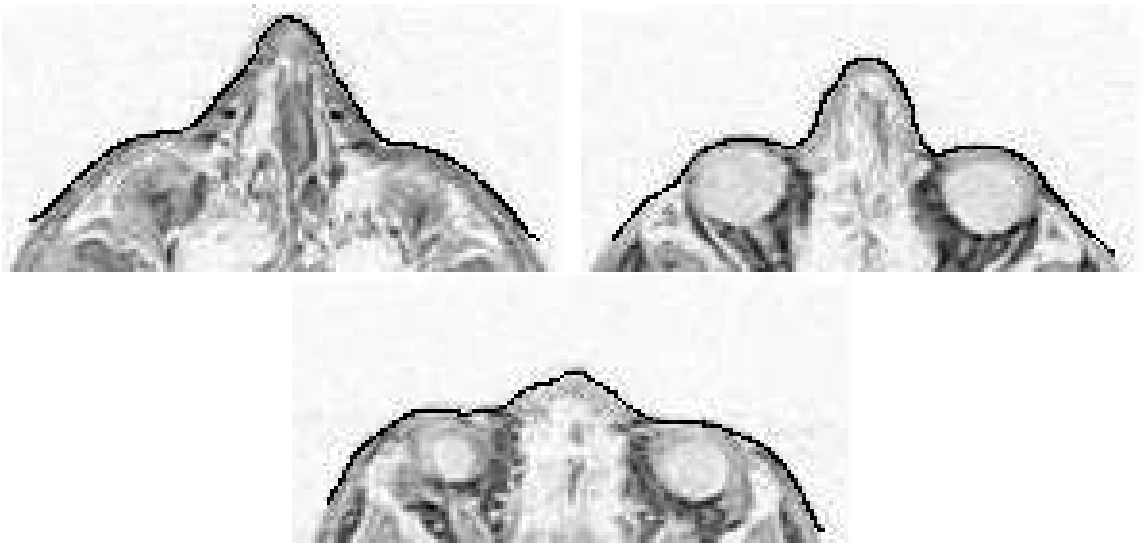

Figure 23: Overlays of some horizontal cross sections of the final surface with the original data.

Appendices

A Surfaces and 3D Edge Points

In this first appendix we give a necessary and sufficient condition for a surface to produce a local extremum of the energy:

$$E_P(\mathcal{S}) = \frac{1}{|\mathcal{S}|}\int P(v(s,r))dA$$

where $|\mathcal{S}| = \int\int |x_s \wedge x_r| dsdr$ and $dA = \sqrt{EG-F^2}dsdr$ is the area element. A necessary and sufficient condition for the surface $\mathcal{S}$ to produce a local extremum of E_P with respect to infinitesimal deformations is:

$$D_{N(v(s,r))}P(v(s,r)) = \frac{eG-2fF+gE}{EG-F^2}\left(P(v(s,r)) - \frac{1}{|\mathcal{S}|}\int\int P(v(s,r))dsdr\right), \qquad (27)$$

and

$$P(v(L,r)) = P(v(0,r)) = \frac{1}{|\mathcal{S}|}\int PdA \quad \forall r \in [0,M] \qquad (28)$$

$$P(v(s,M)) = P(v(s,0)) = \frac{1}{|\mathcal{S}|}\int PdA \quad \forall s \in [0,L] \qquad (29)$$

where $E(s,r)$, $F(s,r)$, $G(s,r)$, $e(s,r)$, $f(s,r)$ and $g(s,r)$ are the coefficients of the first and second fundamental form in the basis $\{x_s, x_r\}$ (see [18] for details about the notations),$\Omega = [0,L]\times[0,M]$.

Let us consider $\mathcal{S}_\lambda$ a small deformation of the surface $\mathcal{S}$ such that the parametrization of $\mathcal{S}_\lambda$ is:

$$x^\lambda = x + \lambda(\alpha x_s + \beta x_r + \gamma N) \qquad (30)$$

where $\alpha(s,r)$, $\beta(s,r)$ and $\gamma(s,r)$ are arbitrary continuous and differentiable functions and $\{x_s, x_r, N\}$ are the derivatives of x and the normal to the surface.

$\mathcal{S}$ is a local extremum of E_P if and only if

$$\left.\frac{dE_P(\mathcal{S}_\lambda)}{d\lambda}\right|_{\lambda=0} = 0 \qquad (31)$$

for all α, β and γ.

We are going to show that (31) holds if and only if (27, 28, 29) are satisfied.

By definition

$$E_P(\mathcal{S}_\lambda) = \frac{\int P(x^\lambda(s,r))dA}{\int dA} = \frac{\int\int P(x^\lambda(s,r))\sqrt{EG-F^2}dsdr}{\int\int \sqrt{EG-F^2}dsdr} \qquad (32)$$

where E, F, and G are the coefficients of the first fundamental form of $\mathcal{S}_\lambda$.

To compute the derivative $\left.\frac{dE_P(\mathcal{S}_\lambda)}{d\lambda}\right|_{\lambda=0}$, we need to compute the derivatives of the vectors x_s, x_r and N. For this purpose we use the following equations (§ 4.3 p. 231 in [18]):

$$x_{ss} = \Gamma^1_{11}x_s + \Gamma^2_{11}x_r + eN$$

$$x_{sr} = x_{rs} = \Gamma^1_{12}x_s + \Gamma^2_{12}x_r + fN$$

$$x_{rr} = \Gamma^1_{22}x_s + \Gamma^2_{22}x_r + gN$$

where the coefficients Γ^k_{ij} are the Christoffel symbols of $\mathcal{S}$ in the parametrization x and e, f, g are the coefficients of the second fundamental form of $\mathcal{S}$. In the following the Christoffel symbols

Γ_{ij}^k have been replaced in terms of the coefficients of the first fundamental form E, F, G and their derivatives.

Thus computing $\dfrac{dE_P(\mathcal{S}_\lambda)}{d\lambda}$ and evaluating it at $\lambda = 0$ leads to:

$$
\begin{aligned}
|\mathcal{S}| \left.\frac{dE_P(\mathcal{S}_\lambda)}{d\lambda}\right|_{\lambda=0} = 0 \quad = \quad & \int\int \sqrt{EG-F^2}\alpha \left[|\mathcal{S}| \frac{dP}{dx_s} + (|\mathcal{S}|\, P - P_m)\left(\Gamma_{11}^1 + \Gamma_{12}^2\right)\right] dsdr \\
& + \int\int \alpha_s \sqrt{EG-F^2}\,(|\mathcal{S}|\, P - P_m)\, dsdr \\
& + \int\int \sqrt{EG-F^2}\beta \left[|\mathcal{S}| \frac{dP}{dx_r} + (|\mathcal{S}|\, P - P_m)\left(\Gamma_{12}^1 + \Gamma_{22}^2\right)\right] dsdr \\
& + \int\int \beta_r \sqrt{EG-F^2}\,(|\mathcal{S}|\, P - P_m)\, dsdr \\
& + \int\int \gamma \left[\sqrt{EG-F^2}\,|\mathcal{S}| \frac{dP}{dN} - (|\mathcal{S}|\, P - P_m) \frac{eG - 2fF + gE}{\sqrt{EG-F^2}}\right] dsdr
\end{aligned}
$$

where $P_m = \int P dA$.

Integrating by parts the integral (except the last one) yields (27) as a necessary and sufficient condition for (31) to be satisfied for all α, β and γ. And evaluating these integrals at the boundaries yields the two additional equations (28) and (29).

B Details of the Numerical Solution

B.1 Variational Formulation

Let $\varphi \in H_0^2([0,1])$ be a smooth function. If v is a solution of Eqn. (15), the associated variational formulation is:

$$
\int_0^1 \frac{\partial v(s,t)}{\partial t}\varphi(s)ds - \int_0^1 \frac{\partial}{\partial s}\left(w_1(s)\frac{\partial v(s,t)}{\partial s}\right)\varphi(s)ds +
$$

$$
\int_0^1 \frac{\partial^2}{\partial s^2}\left(w_2(s)\frac{\partial^2 v(s,t)}{\partial s^2}\right)\varphi(s)ds = \int_0^1 F\left(v(s,t)\right)\varphi(s)ds
$$

We remark that the variables s and t are independents, we can separate them (for more details see [8]). We obtain, using the Green's formula:

$$
\frac{d}{dt}\int_0^1 v(s,t)\varphi(s)ds + \int_0^1 w_1(s)\frac{\partial v(s,t)}{\partial s}\varphi'(s)ds + \int_0^1 w_2(s)\frac{\partial^2 v(s,t)}{\partial s^2}\varphi''(s)ds
$$

$$
= \int_0^1 F\left(v(s,t)\right)\varphi(s)ds
$$

Let us set:

$$
a(\varphi,\psi) = \int_0^1 w_1(s)\varphi'(s)\psi'(s)ds + \int_0^1 w_2(s)\varphi''(s)\psi''(s)ds
$$

and

$$
L_v(\psi) = \int_0^1 F\left(v(s,t)\right)\psi(s)ds
$$

This leads us to a new formulation of the problem: given $v_0 \in L^2(\Omega)$ and $F \in L^2(0,T,L^2(\Omega))$, find a function $v \in L^2(0,T,H_0^2(\Omega)) \cap \mathcal{C}^1(0,T,L^2(\Omega))$ satisfying:

$$
\left\{
\begin{array}{l}
\dfrac{d}{dt}\left(v(t),\psi\right) + a(v(t),\psi) = L_v(\psi)\ \forall \psi \in H_0^2(\Omega) \\
v(0) = v_0 \\
w_1(s), w_2(s) \in L^\infty(\Omega),\ \ w_1(s) \text{ and } w_2(s) \geq \alpha > 0
\end{array}
\right. \tag{33}
$$

We solve the evolution equation but we are in fact interested in the limit when t is large which gives a solution of the static equation:

Find $v \in H_0^2(\Omega)$ such that

$$a(v,\varphi) = L_v(\varphi) \quad \forall \varphi \in H_0^2(\Omega) \tag{34}$$

when L does not depend on v, there exists a unique solution to this equation, since the bilinear form $a(\varphi,\psi)$ is symmetric and positive definite as soon as $w_1(s)$ and $w_2(s) > 0$).

So we solve the evolution equation (33) using an iterative scheme where at each step, L depends only on the estimate of v at the previous step.

In 3D we have to solve the same problem with:

$$a(u,v) = \int_\Omega w_{10}\frac{\partial u}{\partial s}\frac{\partial v}{\partial s} + w_{01}\frac{\partial u}{\partial r}\frac{\partial v}{\partial r} + w_{20}\frac{\partial^2 u}{\partial s^2}\frac{\partial^2 v}{\partial s^2} + 2w_{11}\frac{\partial^2 u}{\partial s \partial r}\frac{\partial^2 v}{\partial s \partial r} + w_{02}\frac{\partial^2 u}{\partial r^2}\frac{\partial^2 v}{\partial r^2}\, dsdr$$

and

$$L_v(u) = \int_\Omega F(v)\, u\, dsdr$$

B.2 V_h Basis Functions in 2D

Using relations (19) and (20) we obtain:

$$\phi_j(x) = \begin{cases} -\frac{2}{h^3}x^3 - \frac{3}{h^2}(1-2j)x^2 + \frac{6j}{h}(1-j)x + 1 + j^2(2j-3) & \text{if } x \in [x_{j-1}, x_j] \\ \frac{2}{h^3}x^3 - \frac{3}{h^2}(1+2j)x^2 + \frac{6j}{h}(1+j)x + 1 - j^2(2j+3) & \text{if } x \in [x_j, x_{j+1}] \\ 0 & \text{elsewhere.} \end{cases} \tag{35}$$

and

$$\Psi_j(x) = \begin{cases} \frac{1}{h^2}x^3 + \frac{1}{h}(2-3j)x^2 + (3j^2-4j+1)x - j(j-1)^2 & \text{if } x \in [x_{j-1}, x_j] \\ \frac{1}{h^2}x^3 - \frac{1}{h}(2+3j)x^2 + (3j^2+4j+1)x - j(j+1)^2 & \text{if } x \in [x_j, x_{j+1}] \\ 0 & \text{elsewhere.} \end{cases} \tag{36}$$

Thus $\forall v_h \in V_h$ we have the identity:

$$v_h = \sum_{i=1}^{N} v_h(x_i)\phi_i + \sum_{i=1}^{N} v_h'(x_i)\Psi_i \tag{37}$$

B.3 Discrete Problem and Linear System in 2D

Rewriting the discrete problem (17) with the basis functions ϕ_i and Ψ_i, give us the equations:

$$\forall j = 1,\ldots,N \quad \begin{cases} a(v_h,\phi_j) = L(\phi_j) \\ a(v_h,\Psi_j) = L(\Psi_j) \end{cases} \tag{38}$$

and using the identity (21), we have:

$$\forall j = 1,\ldots,N \quad \begin{cases} \sum_{i=1}^N v_h(x_i)a(\phi_i,\phi_j) + \sum_{i=1}^N v_h'(x_i)a(\Psi_i,\phi_j) = L(\phi_j) \\ \sum_{i=1}^N v_h(x_i)a(\phi_i,\Psi_j) + \sum_{i=1}^N v_h'(x_i)a(\Psi_i,\Psi_j) = L(\Psi_j) \end{cases} \tag{39}$$

The equation (39) is a linear system, where the unknowns are $v_h(x_i)$ and $v_h'(x_i)$ for $i = 1,\ldots,N$.

Finally the solution of the discrete problem (18) is equivalent to a solution of the linear system:

$$A \cdot V = L$$

where:
- A is a tridiagonal blocs array $A = (A_{ij})_{i,j=1,\ldots,N}$ with:

$$A_{ij} = \begin{pmatrix} a(\phi_i, \phi_j) & a(\Psi_i, \phi_j) \\ a(\phi_i, \Psi_j) & a(\Psi_i, \Psi_j) \end{pmatrix}$$

the A_{ij} array elements depend on the elasticity and rigidity coefficients.
- $V = \left(v_h(x_1), v_h^{'}(x_1), \ldots, v_h(x_N), v_h^{'}(x_N)\right)^T$
- and $L = (L(\phi_1), L(\Psi_1), \ldots, L(\phi_N), L(\Psi_N))^T$.

B.4 Tessellation of Ω and the Basis Functions in 3D

Given the numbers of discretization points in the two axes of parametrization $N_s,\ N_r > 1$, we set $h_s = \frac{1}{N_s - 1},\ h_r = \frac{1}{N_r - 1}$ and consider a uniform subdivision of Ω of step size h_s and h_r, composed of the nodes $a_{i,j} = (s_i, r_j) = (ih_s, jh_r)\ \ 0 \leq i \leq N_s - 1,\ \ 0 \leq j \leq N_r - 1$. Thus

$$\Omega = [0,1] \times [0,1] = \bigcup_{i,j=0}^{N_s-1,N_r-1} K_{i,j} = \bigcup_{i,j=0}^{N_s-1,N_r-1} [ih_s, (i+1)h_s] \times [jh_r, (j+1)h_r]$$

Since the higher derivatives order appearing in the equation (8) are of the fourth order, the finite element space V_h must satisfy $V_h \subset \mathcal{C}^1 \cap H_0^2(\Omega)$ (see for details [8]). For this purpose the space $H_0^2(\Omega)$ is approximated with the Bogner - Fox - Schmit elements [8] defined by:

- The rectangles K_{ij}, defined by the vertices $c_k\ \ 1 \leq k \leq 4$.
- The set $P_{K_{ij}}$of polynomials containing the basis functions:

$$P_{K_{ij}} = Q_3(K_{ij}) = \left\{ p,\ \ p(s,r) = \sum_{0 \leq k,l \leq 3} \gamma_{kl} s^k r^l \right\}$$

- The set $\Sigma_{K_{ij}} = \left\{ p(c_k),\ \frac{\partial p(c_k)}{\partial s},\ \frac{\partial p(c_k)}{\partial r},\ \frac{\partial^2 p(c_k)}{\partial s \partial r} \quad 1 \leq k \leq 4 \right\}$ which allows to define in a unique way the basis functions over each rectangles K_{ij}

The subspace V_h is then defined by:

$$V_h = \{ v \in \mathcal{C}^1(\Omega),\ \ v_{|K_{ij}} \in Q_3(K_{ij}) \}$$

where $Q_k(I)$ is the vector space of the restrictions to an interval $I \subset R^2$ of the polynomials whose degree is less than k for each variable, and $v_{|I}$ is the restriction of the function v to the subset I. The basis functions of the finite element subspace V_h are φ_{ij}, ψ_{ij}, η_{ij} and ζ_{ij} defined in a unique way over each rectangle K_{ij} by:

$$\left\{ \begin{array}{lllllllll} \varphi_{ij}(a_{kl}) & = & \delta_{ij,kl}; & \frac{\partial \varphi_{ij}}{\partial s}(a_{kl}) & = & \frac{\partial \varphi_{ij}}{\partial r}(a_{kl}) & = & \frac{\partial^2 \varphi_{ij}}{\partial s \partial r}(a_{kl}) & = 0 \\ \frac{\partial \psi_{ij}}{\partial s}(a_{kl}) & = & \delta_{ij,kl}; & \psi_{ij}(a_{kl}) & = & \frac{\partial \psi_{ij}}{\partial r}(a_{kl}) & = & \frac{\partial^2 \psi_{ij}}{\partial s \partial r}(a_{kl}) & = 0 \\ \frac{\partial \eta_{ij}}{\partial r}(a_{kl}) & = & \delta_{ij,kl}; & \eta_{ij}(a_{kl}) & = & \frac{\partial \eta_{ij}}{\partial s}(a_{kl}) & = & \frac{\partial^2 \eta_{ij}}{\partial s \partial r}(a_{kl}) & = 0 \\ \frac{\partial^2 \zeta_{ij}}{\partial s \partial r}(a_{kl}) & = & \delta_{ij,kl}; & \zeta_{ij}(a_{kl}) & = & \frac{\partial \zeta_{ij}}{\partial s}(a_{kl}) & = & \frac{\partial \zeta_{ij}}{\partial r}(a_{kl}) & = 0 \end{array} \right. \tag{40}$$

where:

$$\delta_{ij,kl} = \begin{cases} 1 & \text{if } i = k \text{ and } j = l \\ 0 & \text{otherwise} \end{cases}$$

Thus $\forall v_h \in V_h$ we have the identity:

$$v_h = \sum_{i,j=0}^{N_s-1,N_r-1} v_h(a_{ij})\varphi_{ij} + \frac{\partial v_h}{\partial s}(a_{ij})\psi_{ij} + \frac{\partial v_h}{\partial r}(a_{ij})\eta_{ij} + \frac{\partial^2 v_h}{\partial s \partial r}(a_{ij})\zeta_{ij}$$

providing a continuous representation of the solution over the space Ω.

Equations (40) gives the expressions of the basis functions φ_{ij}, ψ_{ij}, η_{ij} and ζ_{ij} represented in Fig. 3. These basis functions can be obtained in a simpler way by a tensorial product of the 2D basis functions ϕ and Ψ (35-36):

$$\begin{cases} \varphi_{ij}(s,r) = \phi_i(s)\phi_j(r), \\ \psi_{ij}(s,r) = \Psi_i(s)\phi_j(r), \\ \eta_{ij}(s,r) = \phi_i(s)\Psi_j(r), \\ \zeta_{ij}(s,r) = \Psi_i(s)\Psi_j(r). \end{cases}$$

B.5 Discrete Problem and Linear System in 3D

Rewriting the discrete problem associated to Eqn. (34) with the basis functions, gives us the four equations: $\forall i, j = 0, \ldots, N_s - 1, N_r - 1$

$$\begin{cases} a(v_h, \varphi_{ij}) = L(\varphi_{ij}) \\ a(v_h, \psi_{ij}) = L(\psi_{ij}) \\ a(v_h, \eta_{ij}) = L(\eta_{ij}) \\ a(v_h, \zeta_{ij}) = L(\zeta_{ij}) \end{cases} \tag{41}$$

and, using the identity (22): $\forall i, j = 0, \ldots, N_s - 1, N_r - 1$

$$\begin{cases} \sum v_h(a_{kl})a(\varphi_{kl}, \varphi_{ij}) + \frac{\partial v_h}{\partial s}(a_{kl})a(\varphi_{kl}, \psi_{ij}) + \frac{\partial v_h}{\partial r}(a_{kl})a(\varphi_{kl}, \eta_{ij}) + \frac{\partial^2 v_h}{\partial s \partial r}(a_{kl})a(\varphi_{kl}, \zeta_{ij}) = L(\varphi_{ij}) \\ \sum v_h(a_{kl})a(\psi_{kl}, \varphi_{ij}) + \frac{\partial v_h}{\partial s}(a_{kl})a(\psi_{kl}, \psi_{ij}) + \frac{\partial v_h}{\partial r}(a_{kl})a(\psi_{kl}, \eta_{ij}) + \frac{\partial^2 v_h}{\partial s \partial r}(a_{kl})a(\psi_{kl}, \zeta_{ij}) = L(\psi_{ij}) \\ \sum v_h(a_{kl})a(\eta_{kl}, \varphi_{ij}) + \frac{\partial v_h}{\partial s}(a_{kl})a(\eta_{kl}, \psi_{ij}) + \frac{\partial v_h}{\partial r}(a_{kl})a(\eta_{kl}, \eta_{ij}) + \frac{\partial^2 v_h}{\partial s \partial r}(a_{kl})a(\eta_{kl}, \zeta_{ij}) = L(\eta_{ij}) \\ \sum v_h(a_{kl})a(\zeta_{kl}, \varphi_{ij}) + \frac{\partial v_h}{\partial s}(a_{kl})a(\zeta_{kl}, \psi_{ij}) + \frac{\partial v_h}{\partial r}(a_{kl})a(\zeta_{kl}, \eta_{ij}) + \frac{\partial^2 v_h}{\partial s \partial r}(a_{kl})a(\zeta_{kl}, \zeta_{ij}) = L(\zeta_{ij}) \end{cases} \tag{42}$$

where all sums are $\sum_{k,l=0}^{N_s-1,N_r-1}$. Equation (42) is a linear system where the unknowns are $v_h(a_{kl})$, $\frac{\partial v_h}{\partial r}(a_{kl})$, $\frac{\partial v_h}{\partial s}(a_{kl})$ and $\frac{\partial^2 v_h}{\partial s \partial r}(a_{kl})$.

Finally the solution of the discrete problem associated to (34) leads to a solution of a linear system: $A \cdot V = L$, where: $A = (\tilde{A}_{ij})_{ij=0,\ldots,Ns-1,Nr-1}$ is a tridiagonal blocs array:

$$\tilde{A}_{ij} = \begin{pmatrix} a(\varphi_{ij}, \varphi_{kl}) & a(\varphi_{ij}, \psi_{kl}) & a(\varphi_{ij}, \eta_{kl}) & a(\varphi_{ij}, \zeta_{kl}) \\ a(\psi_{ij}, \varphi_{kl}) & a(\psi_{ij}, \psi_{kl}) & a(\psi_{ij}, \eta_{kl}) & a(\psi_{ij}, \zeta_{kl}) \\ a(\eta_{ij}, \varphi_{kl}) & a(\eta_{ij}, \psi_{kl}) & a(\eta_{ij}, \eta_{kl}) & a(\eta_{ij}, \zeta_{kl}) \\ a(\zeta_{ij}, \varphi_{kl}) & a(\zeta_{ij}, \psi_{kl}) & a(\zeta_{ij}, \eta_{kl}) & a(\zeta_{ij}, \zeta_{kl}) \end{pmatrix}$$

the $\tilde{A}_{ij}$ array elements depend on the elasticity and rigidity coefficients.